AGU PUBLICATIONS

Geochemistry, Geophysics, Geosystems

RESEARCH ARTICLE
10.1002/2015GC005743

Special Section:
Oceanic Detachment Faults

Heterogeneous and asymmetric crustal accretion: New constraints from multibeam bathymetry and potential field data from the Rainbow area of the Mid-Atlantic Ridge (36°15′N)

Michele Paulatto[1,2], Juan Pablo Canales[3], Robert A. Dunn[4], and Robert A. Sohn[3]

[1]Géoazur, Université Nice Sophia Antipolis, Valbonne, France, [2]Department of Earth Sciences, University of Oxford, Oxford, UK, [3]Department of Geology and Geophysics, Woods Hole Oceanographic Institution, Woods Hole, Massachusetts, USA, [4]Department of Geology and Geophysics, School of Ocean and Earth Science and Technology, University of Hawaii at Manoa, Honolulu, Hawaii, USA

Key Points:
- The style and rate of crustal accretion is asymmetric near NTDs
- Detachment faults nucleate preferentially at offset inside corners
- Faulting increases permeability and hydrothermalism at offsets

Supporting Information:
- Supporting Information S1

Correspondence to:
M. Paulatto,
paulatto@geoazur.unice.fr

Citation:
Paulatto, M., J. P. Canales, R. A. Dunn, and R. A. Sohn (2015), Heterogeneous and asymmetric crustal accretion: New constraints from multibeam bathymetry and potential field data from the Rainbow area of the Mid-Atlantic Ridge (36°15′N), *Geochem. Geophys. Geosyst.*, *16*, doi:10.1002/2015GC005743.

Received 22 JAN 2015
Accepted 5 AUG 2015
Accepted article online 10 AUG 2015

Abstract At slow-spreading mid-ocean ridges, crustal accretion style can vary significantly along and across ridge segments. In magma-poor regions, seafloor spreading can be accommodated largely by tectonic processes, however, the internal structure and formation mechanism of such highly tectonized crust are not fully understood. We analyze multibeam bathymetry and potential field data from the Rainbow area of the Mid-Atlantic Ridge (35°40′N–36°40′N), a section of the ridge that shows diverse accretion styles. We identify volcanic, tectonized and sedimented terrain and measure exposed fault area to estimate the tectonic strain, *T*, and the fraction of magmatic accretion, *M*. Estimated *T* values range from 0.2-0.4 on ridge segments to 0.6-0.8 at the Rainbow nontransform discontinuity (NTD). At segment ends *T* is asymmetric, reflecting asymmetries in accretion rate, topography and faulting between inside and outside offset corners. Detachment faults have formed preferentially at inside corners, where tectonic strain is higher. We identify at least two oceanic core complexes on the fossil trace of the NTD, in addition to the Rainbow massif, which occupies the offset today. A gravity high and low magnetization suggest that the Rainbow massif, which hosts a high-temperature hydrothermal system, was uplifted by a west dipping detachment fault. Asymmetric plate ages indicate localization of tectonic strain at the inside corners and migration of the detachment toward and across the ridge axis, which may have caused emplacement of magma into the footwall. Hydrothermal circulation and heat extraction is possibly favored by increased permeability generated by fracturing of the footwall and deep-penetrating second-generation faults.

1. Introduction

1.1. Crustal Accretion at Mid-Ocean Ridges

Along mid-ocean ridges (MORs), the style of crustal accretion is governed by the balance between heat input from below and heat extraction from above, which are controlled by spreading rate, magmatic input, and hydrothermal activity. In magma-poor regions, or during magma-poor episodes, tectonic extension dominates, causing stretching of the lithosphere and tectonic exhumation of lower crustal and mantle rocks. In magma-rich regions, or during magma-rich episodes, magmatic intrusion at the ridge axis acts to release tensile stresses and limit faulting. The balance between magmatic accretion and tectonic extension can be described by the tectonic strain, *T*, defined as the fraction of lithospheric extension taken up by normal faulting [e.g., *Escartín et al.*, 1999], and by the fraction of magmatic accretion, *M*, defined as the ratio between the spreading rate accommodated by magmatic intrusion and the total spreading rate [e.g., *Buck et al.*, 2005].

At slow spreading ridges crustal accretion style can vary significantly within a single ridge segment, resulting in oceanic crust that is structurally and compositionally heterogeneous. The observed variability is thought to be the result of along-axis variations in melt supply and mantle thermal structure [e.g., *Shaw and Lin*, 1993]. Gravity and seismic tomography studies [*Tolstoy et al.*, 1993; *Hooft et al.*, 2000; *Canales et al.*, 2000; *Seher et al.*, 2010] show that on slow-spreading segments crustal thickness decreases toward the segment ends. The thick oceanic crust found at some segment centers is thought to be primarily generated by magmatic accretion and volcanic extrusion and may be well represented by the classical ophiolite-based model consisting of a layer of extrusive basalt overlying a complex of sheeted dykes and a stack of intrusive

gabbroic cumulate [e.g., *Cann*, 1974]. The oceanic crust generated close to segment ends and in other magma-poor environments is less well understood, but it is thought to be composed predominantly of mixed gabbroic intrusions and variably serpentinized peridotite and to lack an organized layered structure [*Cannat*, 1996; *Karson*, 1998]. In extreme cases volcanic activity can be completely suppressed and the crust can be generated by a combination of magmatic intrusion and tectonic denudation of mantle rocks (non-volcanic spreading) [*Schroeder et al*., 2007]. In this setting the boundary between crust and mantle may not be well defined and in some cases the seismic Moho may correspond to a serpentinization front [*Minshull et al*., 1998].

The decrease in crustal thickness along a spreading segment is often accompanied by a change in the style of faulting, from thin, long, closely spaced faults at the segment center to larger and wider-spaced faults at the segment ends [e.g., *Shaw*, 1992]. Since the far field extensional stress does not vary significantly between segment centers and segment ends, it was thought that the variation of faulting style was determined by changes in the thermal structure and rheology of the lithosphere, with thicker, cooler and stronger lithosphere at the segment ends being able to support larger faults [e.g., *Shaw and Lin*, 1993; *Searle and Escartín*, 2004]. On the other hand, numerical models of extension with elasto-plastic rheology [*Behn and Ito*, 2008; *Tucholke et al*., 2008] indicate that, although elastic properties play a role, the main factor in determining faulting style is the fraction of magmatic accretion, *M*. According to this model, *M* controls the rate at which faults are rafted off axis and how stresses accumulate and are released at the ridge and therefore determines the tectonic strain, *T*, and the style of faulting. A high *M* ($>$ 0.5) gives rise to regular closely spaced bookshelf style faults. At *M* close to 0.5, stable long-lived faults (detachment faults) are predicted to develop on one side of the ridge, giving rise to striated mounds exposing lower crustal and mantle rocks (oceanic core complexes, OCC). For $M < 0.5$, fault spacing and size decreases again, producing a smooth but irregular terrain consisting mostly of exposed fault surfaces (tectonized seabed) [*Cannat et al*., 2006]. Since at slow-spreading ridges melt input tends to be focused at segment centers, *M* generally decreases away from the centers leading to higher tectonic strain and larger faults at segment ends.

The ratio *M* is a useful parameter for characterizing and understanding numerical models, however it cannot be easily measured in the field. The tectonic strain, *T*, on the other hand, can be estimated from analysis of swath bathymetry in areas close to the ridge [e.g., *Escartín et al*., 1999]. The relationship between *M* and *T* is not straightforward, since *M* is an integrated quantity over the full crustal thickness, while *T* is measured at the seabed. In an ideal scenario where all of the magmatic accretion occurs by vertical diking within a narrow accretionary zone, *T* and *M* are reciprocal (i.e., $T = 1\text{-}M$). However, it is well established that a significant portion of magmatism is intruded directly into footwalls [e.g., *Dick et al*., 2000; *Grimes et al*., 2008], making estimates of *M* from morphological data a biased measure of magmatic accretion fraction in the absence of additional constraints on deep footwall structure. When discussing the dynamics of detachment faults, *MacLeod et al*. [2009] make a distinction between magma delivered to the hanging wall, which determines the magmatic contribution to plate separation, M_{HW}, and magma delivered into the footwall, M_{FW}. The ratio *M* used in the numerical models [*Buck et al*., 2005; *Behn and Ito*, 2008; *Tucholke et al*., 2008] is equivalent to M_{HW} and can be estimated to first order assuming it is equivalent to the nontectonic strain, *1-T*, measured at the seabed. *M* can therefore be thought of as the fraction of total magmatic input that contributes to building new seabed through diking and volcanic extrusion and may be better named the *fraction of volcanic accretion*.

The Mid-Atlantic Ridge (MAR) has a tectonic strain, *T*, which is generally between 0.2 and 0.6, but can be locally close to 1.0 [*Dick et al*., 2008; *Behn and Ito*, 2008; *Grimes et al*., 2008] and has therefore the potential to exhibit all three types of faulting behavior (i.e., close-spaced bookshelf faulting, detachment faulting and smooth tectonized seabed). In this study we use newly acquired multibeam bathymetry and potential field data [*Canales et al*., 2013] to investigate the spatial and temporal variability of faulting style, magmatic input and lithospheric properties on the MAR between 35°40′N and 36°40′N, a ridge section that includes the Rainbow nontransform discontinuity (NTD) and the Rainbow ultramafic massif and associated hydrothermal field [e.g., *Gràcia et al*., 2000]. Our results constrain the dynamics of crustal accretion and the relationship between detachment faulting, magmatism and hydrothermal activity along this MAR section.

1.2. The MAR Between 35 and 37°N and the Rainbow Hydrothermal Field

The section of the MAR between 35°40′N and 36°40′N is spreading at a full rate of 22 mm/yr with an average azimuth of 104° [*DeMets et al*., 2010]. The overall magmatic input, as indicated by gravity and seafloor

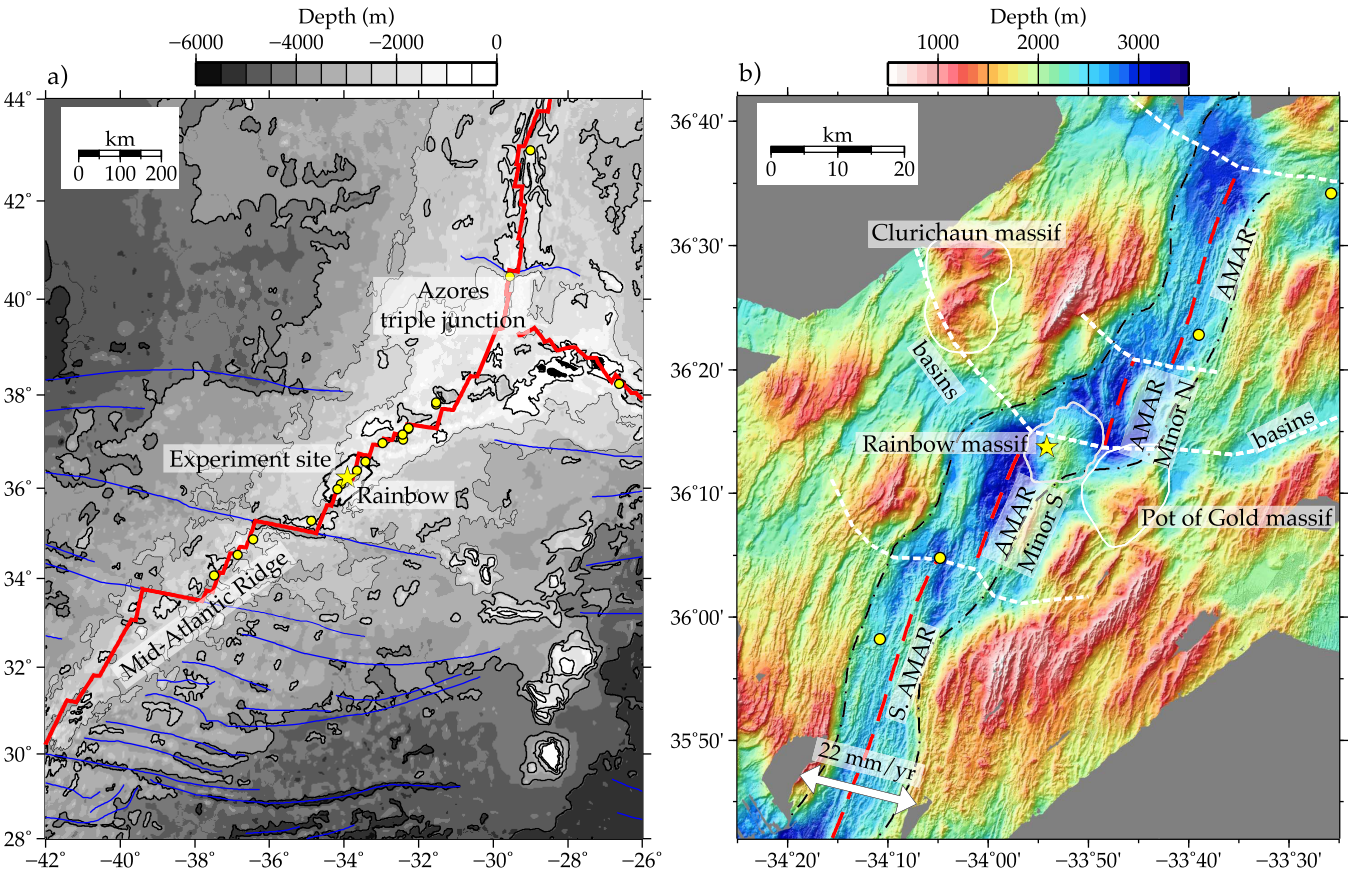

Figure 1. (a) Bathymetric map of the Mid-Atlantic Ridge showing the experiment site, the ridge axis (red) and major fracture zones (blue). (b) Bathymetric map of the survey area. The Rainbow massif and other massifs interpreted as remnants of core complexes are outlined in white. The ridge axis is marked with a red dashed line. Its location was determined from the analysis of the bathymetry and potential field data. Note the three ridge offsets. A dashed/dotted line marks the axial valley walls. Dashed white lines mark the boundaries between ridge segments. The rainbow hydrothermal field is marked with a yellow star. The location of other identified hydrothermal sites or plumes are marked with yellow circles (InterRidge Vents Database 3.2, http://vents-data.interridge.org/). A white arrow marks the spreading vector direction.

depth, is elevated compared to sections of the ridge to the south, because of the influence of the nearby Azores hotspot [*Detrick et al*., 1995; *Thibaud et al*., 1998; *Parson et al*., 2000], and this results in a shallower ridge (Figure 1a). The average orientation of the plate boundary is ~60° clockwise from north and there is a ~16° difference between the spreading vector and the direction perpendicular to the average strike of the plate boundary. On the other hand, the ridge is divided into a series of mostly right-stepping ridge segments whose strikes are rotated counter-clockwise to the average strike of the plate boundary; as such, their individual orientations are only a few degrees different from the direction perpendicular to their spreading vectors. NTDs comprise the majority of the offsets between ridge segments in this region, including the Rainbow NTD, a 12 km wide offset characterized by nonvolcanic spreading. Previous studies recognized three ridge segments in our study area: S. AMAR, AMAR Minor and AMAR segments [e.g., *German et al*., 1996].

The Rainbow NTD is a second order offset [*Grindlay et al*., 1991] or Type 1 NTD, also termed a "septal offset" [*Spencer et al*., 1997], i.e., a discontinuity marked by a topographic ridge separating the two segment ends. The topographic ridge, known as the Rainbow massif, is dome-shaped with a surface composed of ultramafic rocks intermixed with gabbroic intrusions and variously covered by a veneer of pelagic and hydrothermal sediment [*Andreani et al*., 2014]. It has been suggested that the Rainbow massif is an oceanic core complex, as indicated by its dome shape, its predominantly ultramafic surface composition, and its associated Bouguer gravity anomaly high [*Fouquet et al*., 1997; *Andreani et al*., 2014]. The massif hosts a major hydrothermal vent field, the Rainbow hydrothermal field (RHF), composed of several black smokers and other vents, which emit H_2 and CH_4-rich fluids at temperatures of up to ~365°C and flow rates up to 450 L/s [*Charlou et al*., 2002; *German et al*., 2010]. The high temperature and high flow rate suggest that the system

is driven by a magmatic heat source [*Cann and Strens*, 1982; *Allen and Seyfried*, 2004], however crustal accretion in the area appears dominated by tectonic extension and is free of extrusive volcanic morphologies. The lifetime of the RHF is difficult to constrain, but sediment sample data [*Cave et al*., 2002] and Th/U dating of black smoker chimneys [*Kuznetsov et al*., 2006] suggest that it has been active for at least ~23 kyr. Such a long time scale seems to require a magmatic source that is also relatively stable in the medium term, but magma supply is likely to be episodic in the long term since long-term magmatic input should be very low at NTDs [e.g., *Cannat et al*., 1995; *Phipps-Morgan and Forsyth*, 1988].

2. Data Acquisition, Processing, and Analysis

Data for this study were collected in May–June 2013 as part of the MARINER (Mid-Atlantic Ridge INtegrated Experiments at Rainbow) marine geophysical survey of the Rainbow area [*Dunn et al*., 2013; *Canales et al*., 2013], a set of acoustic mapping, potential field mapping, and seismic imaging studies of the area surrounding the RHF. The main aims were to understand crustal accretion along the spreading segments and within the NTD, and the relationship between magmatic input, faulting and hydrothermal activity. The experiment collected wide-angle and multichannel seismic data along closely spaced profiles that spanned the Rainbow NTD and adjacent ridge segments. Concurrently, multibeam bathymetry, gravity and magnetic data were collected along those lines (Figure S1). The seismic data will be presented elsewhere, here we present the bathymetry and potential field data and results.

2.1. Swath Bathymetry

The swath bathymetry data were collected with a Kongsberg EM-122 multibeam system along closely-spaced profiles which provided redundant coverage over most of the survey area. The data were merged with existing data from previous cruises [*Needham et al*., 1991; *Detrick et al*., 1995; *Cannat et al*., 1999], with priority given to the MARINER data. The high density of soundings allowed gridding at a relatively fine grid interval of 0.00025°×0.00025° (~25 m grid spacing) (see supporting information Figure S1). The resulting grid covers a 70 × 110 km^2 area of the seabed (Figure 1b).

To aid the interpretation of geomorphological features we calculated a range of morphometric functions from the bathymetric grid, including slope gradient, terrain illumination and roughness [*Wilson et al*., 2007; *Micallef et al*., 2007] using tools from GMT [Generic Mapping Tools, *Wessel et al*., 2013], Fledermaus [http://www.qps.nl/display/fledermaus], GRASS [http://grass.osgeo.org] and GDAL [http://www.gdal.org/]. The slope gradient (Figure 2a) can be used to identify faults [e.g., *Shaw and Lin*, 1993], since they generally have steeper slopes (30° – 60°) than volcanic features. However in areas where crustal accretion is significantly tectonized, long-lived slip on detachment faults can cause large footwall rotation and produce fault angles as low as 10° – 20° [*Smith et al*., 2008]. The slope map was therefore inspected in conjunction with the roughness map (Figure 2b) to identify shallow dipping but smooth terrain corresponding to low-angle detachment faults. Roughness is defined as the maximum of the differences between a central grid node and the surrounding nodes [*Wilson et al*., 2007]. Other identified features include volcanic ridges, cones and mounds, tectonized patches and sediment-covered areas.

We also used an automatic edge detection algorithm [*Canny*, 1986] to identify lineaments in the bathymetry (Figure 2c) and guide fault identification and the classification of terrain type. This method is based on the identification of connected local maxima in the gradient of the input grid. The algorithm uses two threshold values for maxima identification to detect strong and weak edges. Weak edges are output only if they are connected to strong edges. We use the slope gradient as input to the algorithm; therefore it effectively works on the curvature of the bathymetry, identifying linear ridges and troughs. Maps of average lineament orientation and its standard deviation within overlapping 0.1 x 0.1 degree cells (Figure 2d) give an unbiased indication of the spatial variability of the style of faulting.

2.2. Gravity Analysis and Modeling

The gravity data were recorded with a Bell Aerospace BGM-3 marine gravimeter. The data were corrected for the Eötvös effect and instrument drift and were reduced to free-air gravity anomaly (Figure 3a and supporting information). The swath bathymetry grid was merged with satellite-derived bathymetry to fill in holes in the swath grid and was then used to calculate the Bouguer correction using the spectral method of *Parker* [1973]. We used a water density of 1030 kg/m^3 and a crustal density of 2700 kg/m^3. The Bouguer

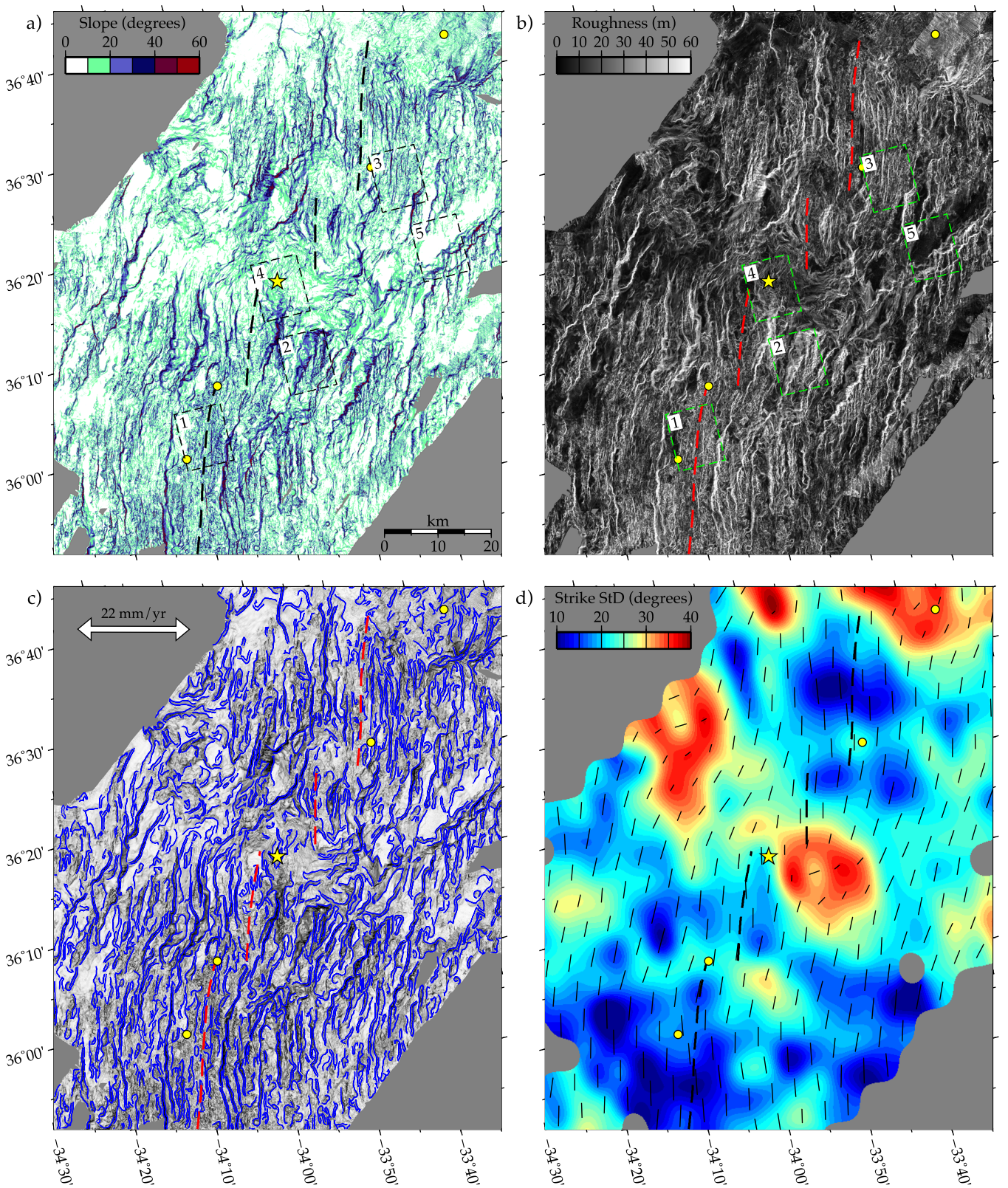

Figure 2. Morphometric maps calculated from the multibeam bathymetry grid. In all plots the projection is rotated to align the horizontal with the spreading direction. (a) Slope gradient. (b) Roughness. (c) Seabed lineaments drawn from the slope map using an edge detection algorithm. The slope gradient is plotted for reference in the background with a gray color scale. (d) Standard deviation of the lineament strike within 0.1°×0.1° cells. This map highlights areas where the seabed fabric lacks organized alignment. Superimposed black bars show local average of lineament direction. A thick dashed line marks the ridge axis. The Rainbow hydrothermal field is marked by a yellow star. Other identified hydrothermal sites and plumes are marked by yellow circles. Numbered dashed boxes correspond to areas shown in Figure 5.

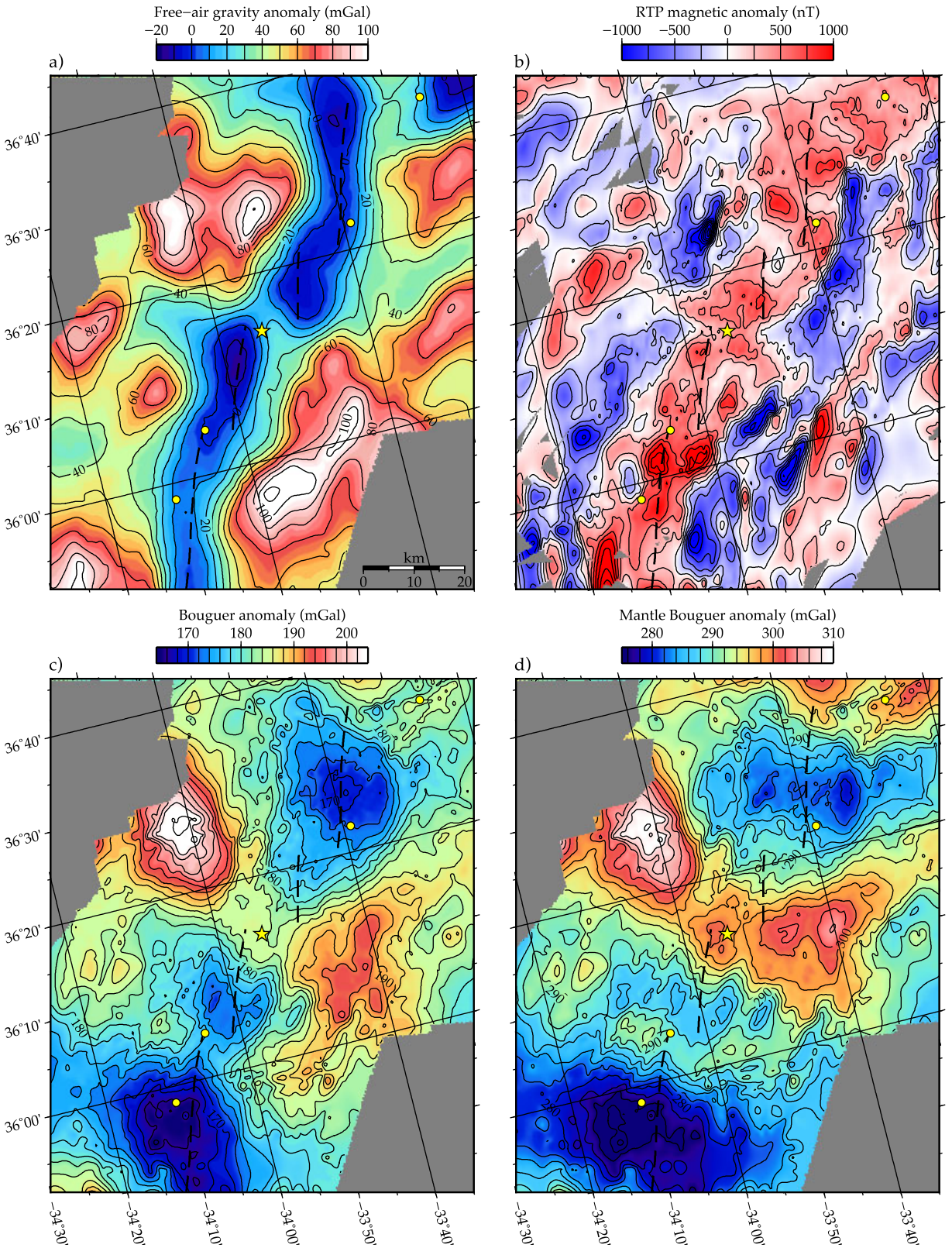

Figure 3. Analysis of the potential field data. (a) Free-air gravity anomaly at the sea surface calculated from shipboard gravity data. (b) Reduced-to-pole magnetic anomaly. (c) Bouguer gravity anomaly assuming a crustal density of 2700 kg/m^3. (d) Mantle Bouguer anomaly assuming a 400 kg/m^3 density contrast at 4.5 km depth below the seabed. In all plots the map projection is rotated to align the horizontal with the spreading direction. A dashed black line marks the ridge axis. The Rainbow hydrothermal field is marked by a yellow star. Other identified hydrothermal sites and plumes are marked by yellow circles.

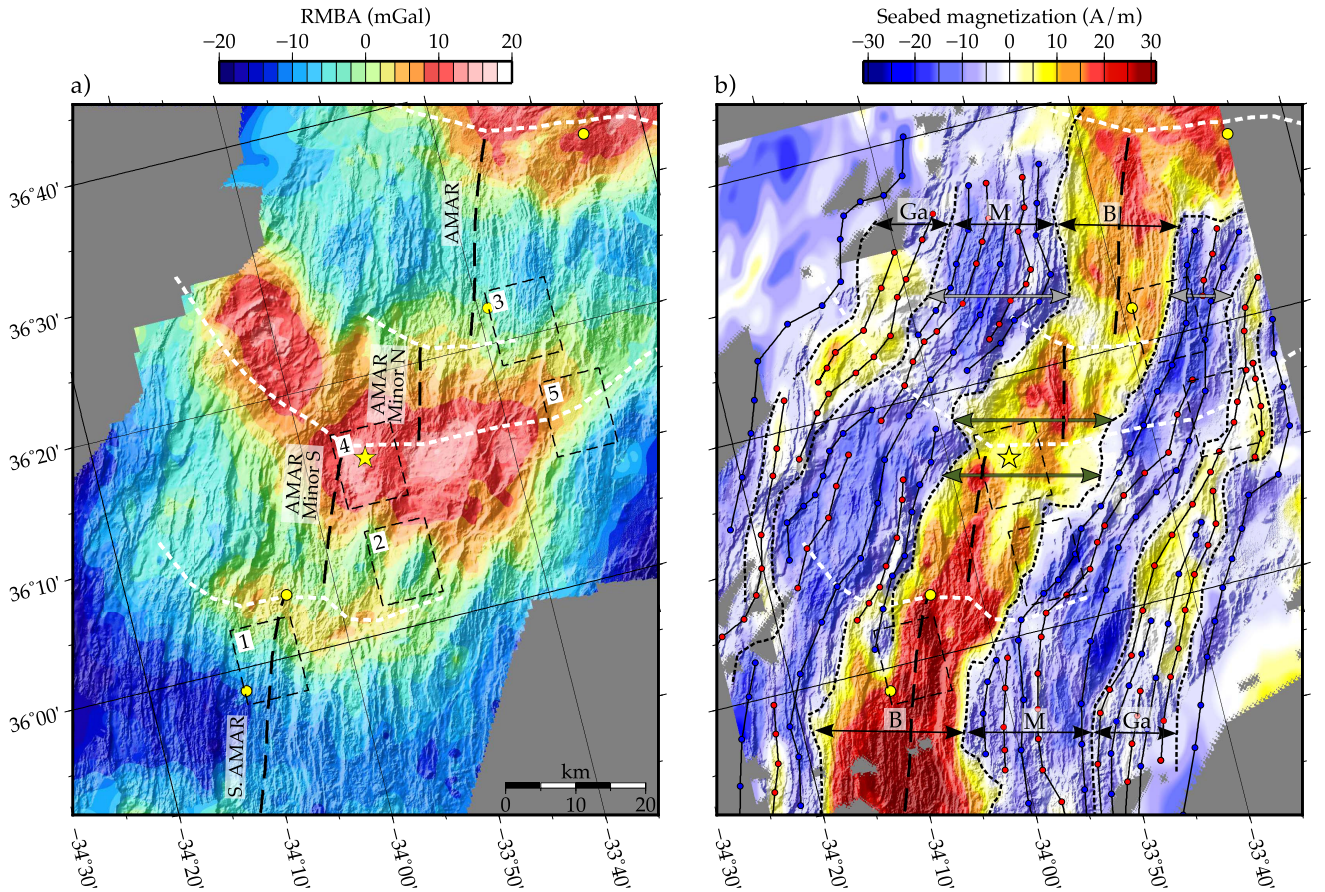

Figure 4. (a) Residual Mantle Bouguer Anomaly (RMBA) with superimposed terrain illumination calculated from the bathymetry grid. (b) Seabed magnetization calculated from inversion of the magnetic anomaly assuming a constant thickness source layer (500 m). Again the terrain illumination is superimposed on the color map. Dashed black curves mark the magnetic reversals between major magnetic chrons (B=Brunhes, M=Matuyama, Ga=Gauss). Normal polarity chrons are marked by black lines with red dots. Reverse polarity chrons are marked by black lines with blue dots. The magnetic chrons were picked from laterally continuous local maxima and minima in the magnetization map with aid from the geomagnetic timescale of *Gee and Kent* [2007]. In both plots, the map projection is rotated to align the horizontal with the spreading direction. A dashed black line marks the ridge axis. Dashed white lines mark the boundaries between ridge segments. The Rainbow hydrothermal field is marked by a yellow star. Other identified hydrothermal sites and plumes are marked by yellow circles. Areas shown in Figure 5 are marked by dashed boxes.

correction was subtracted from the free-air gravity anomaly to obtain the Bouguer gravity anomaly (BA) (Figure 3c).

We then calculated the mantle Bouguer correction [*Kuo and Forsyth*, 1988], assuming a 4.5 km constant-thickness crust and densities of 2900 kg/m^3 and 3300 kg/m^3 for the crust and upper mantle respectively. The mantle Bouguer correction was subtracted from the BA to obtain the mantle Bouguer anomaly (MBA) (Figure 3d). Initial results from the MARINER seismic data [*Dunn et al*., 2014] indicate an average crustal thickness across the study area of about ~4.5 km, but without a sharp crust-mantle boundary. The seismic tomography results also indicate significant lateral and vertical variations in elastic properties in this area, which may be due to changes in porosity and chemical alteration with depth as well as changes in composition. Across the area of the NTD that contains the Rainbow massif, crustal material may be very thin, nonexistent, or variably mixed with mantle material. The MBA, will reflect these and other deviations from the applied assumption of a simple constant-thickness crustal layer.

A large component of the MBA is expected to arise from an across-axis temperature gradient in the upper mantle due to upwelling beneath the ridge axis and plate cooling. We estimate the gravity contribution of the mantle thermal structure and subtract it from the MBA to obtain the residual mantle Bouguer anomaly (RMBA) (Figure 4a). We use a simple model of passive mantle upwelling driven from the top by plate divergence at the ridge axis [*Phipps-Morgan and Forsyth*, 1988] to estimate the 3D temperature structure of the mantle and its gravity contribution [e.g., *Georgen et al*., 2001; *Smith et al*., 2008].

2.3. Magnetic Anomalies and Seabed Magnetization

The magnetic data were recorded with a towed Geometrics G-882 cesium vapor magnetometer along a series of profiles during the seismic experiment. They were corrected for the instrument layback, filtered to remove short-wavelength noise and reduced to magnetic anomalies by removing the International Geomagnetic Reference Field (IGRF). The resulting values were merged with data from previous cruises available from the NGDC and Sismer databases [*Tivey and Dyment*, 2010] and were gridded with a spacing of 0.002 degrees (see supporting information Figure S1). The anomalies were reduced to the pole using an FFT method [*Parker and Huestis*, 1974] (Figure 3b).

We use an FTT method [*Parker and Huestis*, 1974; *MacDonald et al*., 1980] to invert the unreduced magnetic anomaly for seabed magnetization (Figure 4b). The method operates on 2D gridded data and assumes a magnetized layer of constant thickness (500 m) with upper boundary defined by the bathymetry [*Tivey and Tucholke*, 1998]. Magnetization is laterally variable but constant with depth. The magnetization vector is assumed to be parallel to the local direction of the geocentric dipole. To ensure convergence, the data were band-pass filtered between 250 and 2.5 km.

3. Results

Our bathymetry and potential field maps extend from the southern end of the S. AMAR segment (35°40′N) to the northern end of the AMAR segment (36°40′N). The large-scale morphology is typical of slow spreading ridges and consists of a deep axial valley, delimited by generally well-defined valley walls and marked by a free-air gravity anomaly low. We picked the ridge axis based on the location of the minimum in the free-air gravity anomaly, the youngest-looking volcanics and the maximum in seabed magnetization. This is necessarily a subjective choice since crustal accretion is not localized in an infinitely narrow zone, but involves a broader area within the axial valley. This section of the ridge is offset in three places: at the Rainbow NTD, at the S. AMAR/AMAR Minor NTD (hereafter referred to as the S. AMAR NTD), and by a small previously unrecognized NTD, which splits the AMAR segment into two subsegments (the AMAR NTD). Here we refer to the AMAR segment to indicate the major northern subsegment of what was previously known as the AMAR segment and to the AMAR Minor N segment to indicate the southern subsegment. For consistency we refer to the AMAR Minor S segment to indicate what was previously known as the AMAR Minor segment (Figure 1b). The region is characterized by strong variations in morphology and potential field anomalies both along- and across-axis and by marked asymmetries which are described below.

3.1. Gravity Anomalies

The BA and MBA maps (Figures 3c and 3d) show characteristic bull's eye patterns centered on the mid points of the major ridge segments [e.g., *Kuo and Forsyth*, 1988], which likely arise from the combined effect of along-axis crustal thickness variations and across-axis lithospheric cooling. The first-order thermal effect had been removed in the RMBA anomaly (Figure 4a), which therefore can be interpreted in terms of crustal thickness and compositional variations, and possibly second-order thermal variations. RMBA lows are present at the segment centers and correspond to areas characterized by shallower axial valley depth, as compared to ridge segment ends, and hummocky seafloor created by extrusive volcanism and strong magmatic input. By inference, the RMBA lows are consistent with thicker crust and possibly elevated upper mantle and/or crustal temperatures. In contrast, RMBA highs are found near ridge offsets. In particular, across the Rainbow NTD there is a strong and broad RMBA high that extends off-axis to lithospheric ages of at least 3.5 Myr. A strong local RMBA high is associated with the Rainbow massif itself, and is centered over its western flank and slightly offset to the northwest with respect to the topographic high, indicating extensive crustal thinning or low crustal production. A weak RMBA high is also present over the S. AMAR NTD, suggestive of a reduced melt supply in this area. Other small-scale RMBA anomalies associated with faulting are discussed below in conjunction with the geomorphological analysis.

3.2. Seabed Magnetization

To first order, the magnetic anomaly and seabed magnetization maps (Figures 3b and 4b) show two parallel areas with a strongly negative anomaly encompassing a positive anomaly following the central valley of the ridge. We identified magnetic isochrons on the magnetization map using the geomagnetic timescale of *Gee and Kent* [2007] up to chron C2Ar (3.58 – 4.18 Ma). The central positive anomaly corresponds to seafloor

younger than the Bruhnes-Matuyama magnetic field reversal (0.78 Ma). The Matuyama-Gauss reversal (2.58 Ma) can be identified at 20–35 km distance from the ridge (Figures 3b and 4b), leading to a local half-spreading rate estimate of 7.8–13.6 mm/yr, in agreement with the regional half-spreading rate of 11 mm/yr [*DeMets et al*., 2010].

The western flank of the Rainbow massif, which includes the RHF, is characterized by relatively low magnetization, which could reflect exhumation of ultramafic lower-crustal or mantle rocks with inherently lower magnetization than extrusive basalt. Ultramafic rocks that are significantly serpentinized can have appreciable magnetic susceptibility, since serpentinization reactions generate magnetite [e.g., *Tivey and Dyment*, 2010], however measured magnetic susceptibility and natural remanent magnetization of serpentinized peridotite samples from the Rainbow massif are weak [*Szitkar et al*., 2014]. The strongest observed magnetization, likely corresponding to young extrusive volcanic structures, is found within the axial valley near the S. AMAR segment center.

3.3. Seabed Morphology

Inspection of the slope, roughness and lineament maps allows the identification of three main morphological classes:

1. Extrusive volcanic morphology is characterized by small-scale irregular hummocky morphology consisting of lava flows and cones with a diameter of a few tens to a few hundred meters and sometimes larger and smoother flat-topped or cratered cones. (Figure 5, columns 1–3).
2. Exposed fault morphology is smoother but irregular and lacks the small cones and lava flows. It is generally characterized by a lower roughness and a consistent inward-facing slope that can be strongly affected by mass wasting (Figure 5, columns 2 and 4).
3. Sedimented areas are flat and smooth, with very low roughness, and are found mostly off axis within topographic depressions (Figure 5, column 5).

Volcanic, faulted and sedimented morphologies are found throughout the survey area in different proportions. Volcanic morphology is the most common type of seabed morphology and is found both within the axial valley and on the ridge flanks, predominantly near the centers of the AMAR and S. AMAR segments and on the AMAR Minor S segment. There are differences in the morphology of the extrusive volcanics in the axial valley between the segments, reflecting changes in magmatic input. On the S. AMAR segment we find a well-defined axial valley, with a large axial volcanic ridge (AVR) as previously observed by *Parson et al*. [2000] and indicating vigorous magma supply. The AMAR segment has a flat valley floor covered in hummocky volcanic ridges of smaller volume. On the AMAR Minor S segment we observe mainly smooth flows and larger isolated mounds and cones (Figures 2 and 6), indicating a lower or episodic magma supply [*Colman et al*., 2012]. The AMAR Minor N segment seems almost free of recent extrusive volcanics.

Exposed fault morphologies include clear fault surfaces and broad areas of smooth seafloor similar to those observed on the Southwest Indian Ridge [*Cannat et al*., 2006; *Sauter et al*., 2013]. Faults are characterized by smooth surfaces and dipping slopes, and they are delimited by a sharp ridge (the breakaway ridge) on one side and sometimes a sharp hanging wall cutoff on the other side.

3.4. Fault Characteristics

The centers of major segments are characterized by regular parallel faults (*mode C faults*, which appear to develop at the segment center and propagate outward [*Behn et al*., 2002]). Here faults are generally small and closely spaced, but their size and spacing vary along the segments and sometimes between conjugate ridge flanks (Figures 2, 5, and 6a). For example, the east flank of the AMAR segment is finely faulted while the west flank is not so finely faulted and exhibits more uplift. In the south, the S. AMAR and AMAR Minor S segments tend to have larger, wider-spaced faults (Figures 6a and 6b). Fault characteristics also vary with distance from the ridge axis. In particular on the flanks of the AMAR Minor S segment we observe an alternation of large faults with sets of smaller faults (Figure 6a).

Moving from the segment centers toward the inside corners of the Rainbow NTD we find a predominance of faults with larger heave and separation, corresponding to *mode E faults* (faults which develop at segment ends and propagate inward [*Behn et al*., 2002]), and the axial valley deepens to form nodal basins (Figures 1b and 6d). Away from the segment centers faults tend to become less steep (Figure 6b). Large mode E

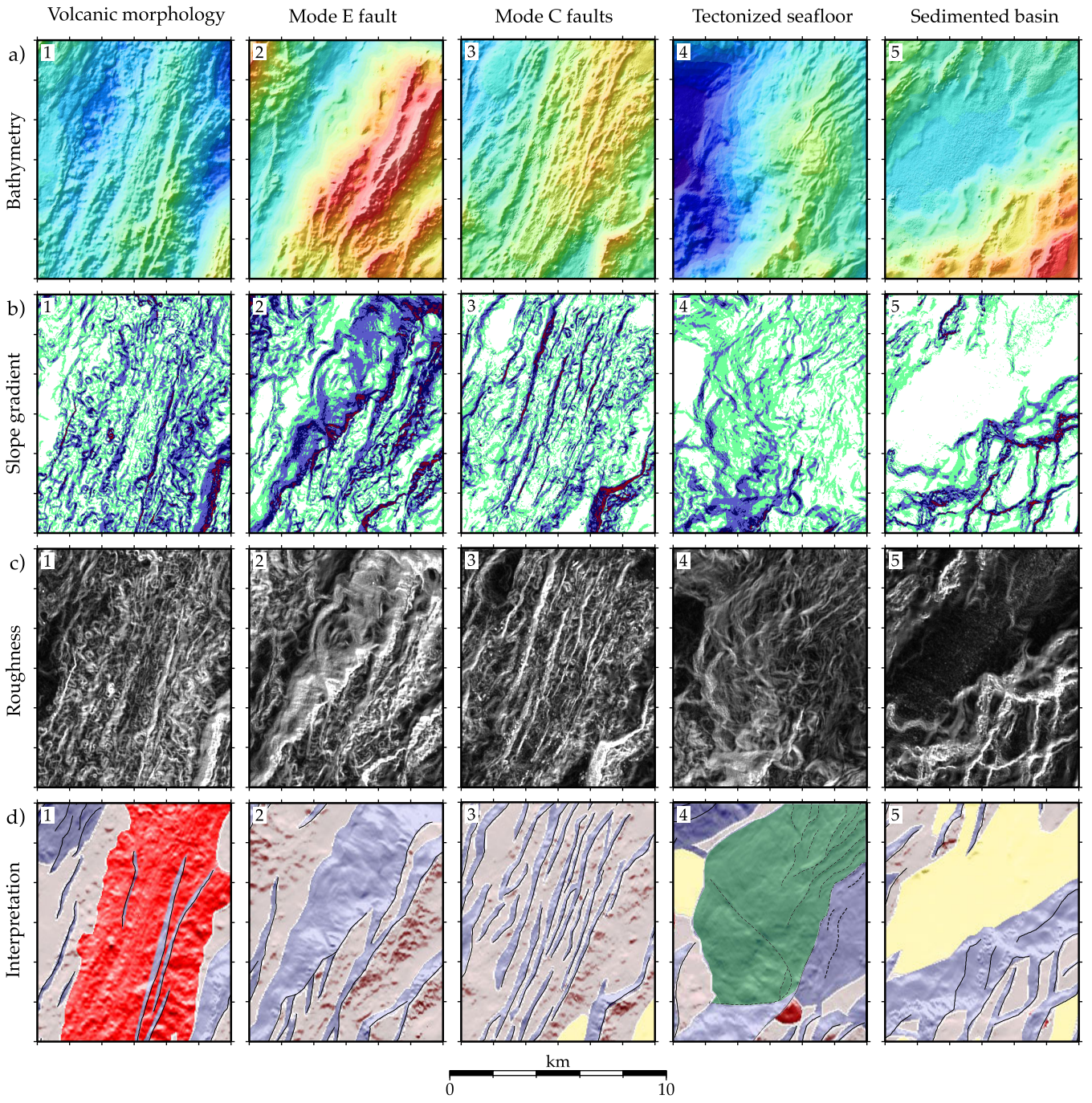

Figure 5. Detail of morphological features. (a) Elevation with terrain illumination from the NW, color scale as in Figure 1a. (b) Slope gradient, color scale as in Figure 2a. (c) Roughness, color scale as in Figure 2b. (d) Geological interpretation, color scale as in Figure 6a. Column 1: Example of volcanic morphology on the axial volcanic ridge; column 2: large mode E fault and back-tilted volcanics; column 3: mode C faults and volcanic terrain; column 4: tectonized seafloor including the Rainbow massif; column 5: sediment-filled basin and interlinked faults.

faults are also found near the inside corners of the two smaller NTDs and are particularly evident in the bathymetry of the AMAR Minor S segment (Figures 2, 5, and 6) where they are associated with axis-parallel bands in both the magnetization and the RMBA (Figure 4).

At and near the Rainbow NTD the seabed seems to consist mostly of exposed fault surfaces (Figures 6a and 6c). Topographic highs associated with local RMBA highs, low magnetization and smooth seabed morphology are interpreted as exposed detachment fault surfaces forming OCCs. We identify at least two possible OCCs in addition to the Rainbow massif. An exposed detachment fault with subtle corrugations parallel to

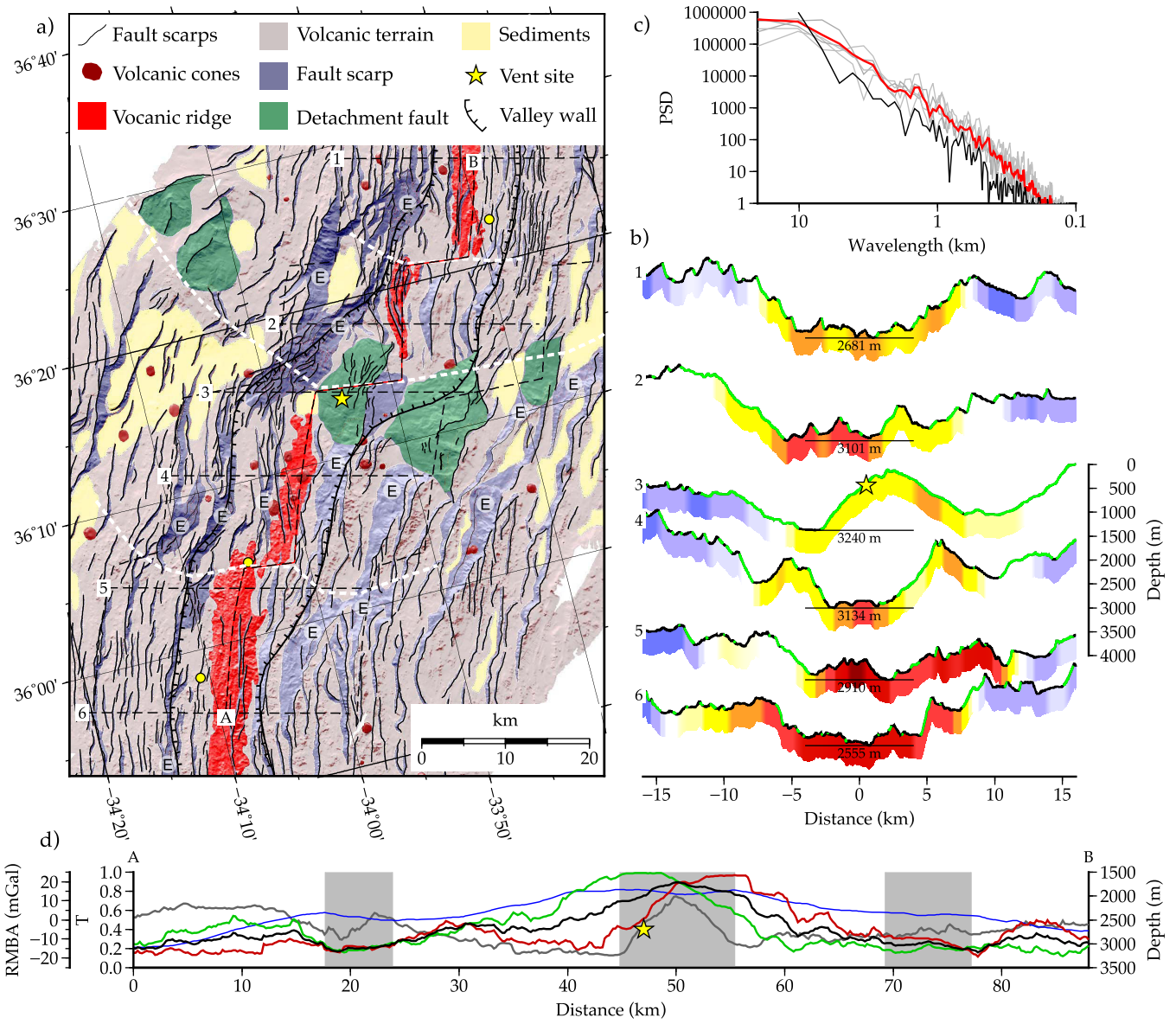

Figure 6. (a) Map interpretation of the Rainbow area. The map projection is rotated to align the horizontal with the spreading direction. Major mode E faults are marked (E). The profiles shown in Figures 6b and 6d are marked by black dashed lines. Dashed white lines mark the boundaries between ridge segments. (b) Across axis profiles of bathymetry. Green sections correspond to exposed fault surfaces identified in Figure 6a. The seabed magnetization extracted from the grid shown in Figure 4b is drawn beneath each profile (same color scale). (c) Power spectral density of the profiles shown in Figure 6b. A thicker black line marks the spectrum of the profile crossing the Rainbow massif, which shows a reduced short wavenumber component. The average of all other profiles is drawn in red. d) Along-axis profile (AB) of bathymetry (gray), RMBA (blue) and tectonic strain, *T*, (black). *T* is calculated over profiles extracted every 200 m along AB and extending 16 km off-axis in either direction parallel to the far-field spreading vector and to the profiles shown in (b). Red curve shows *T* calculated on W flank only; green curve shows *T* for E flank only.

the spreading direction is observed on the flank of an asymmetric dome-shaped topographic high found 15 km off axis southeast of the Rainbow NTD (the Pot of Gold massif, Figures 1b, 7b, and 7d). Another area of elevated and irregular topography interpreted as comprising at least two exposed detachment faults is observed northwest of the NTD, 20 to 40 km off-axis (the Clurichaun massif, Figures 1 and 6). All observed detachment faults and other large faults in the area are found at the inside corners of NTDs.

Faults near segment centers strike approximately NNE-SSW, but are rotated clockwise to a more E-W orientation close to the Rainbow NTD. Seabed lineaments are also rotated near the two smaller NTDs in association with mode E faults and are strongly disrupted on the identified OCCs. Even at the segment centers there is a discrepancy of a few degrees between the average lineament orientation, which is approximately

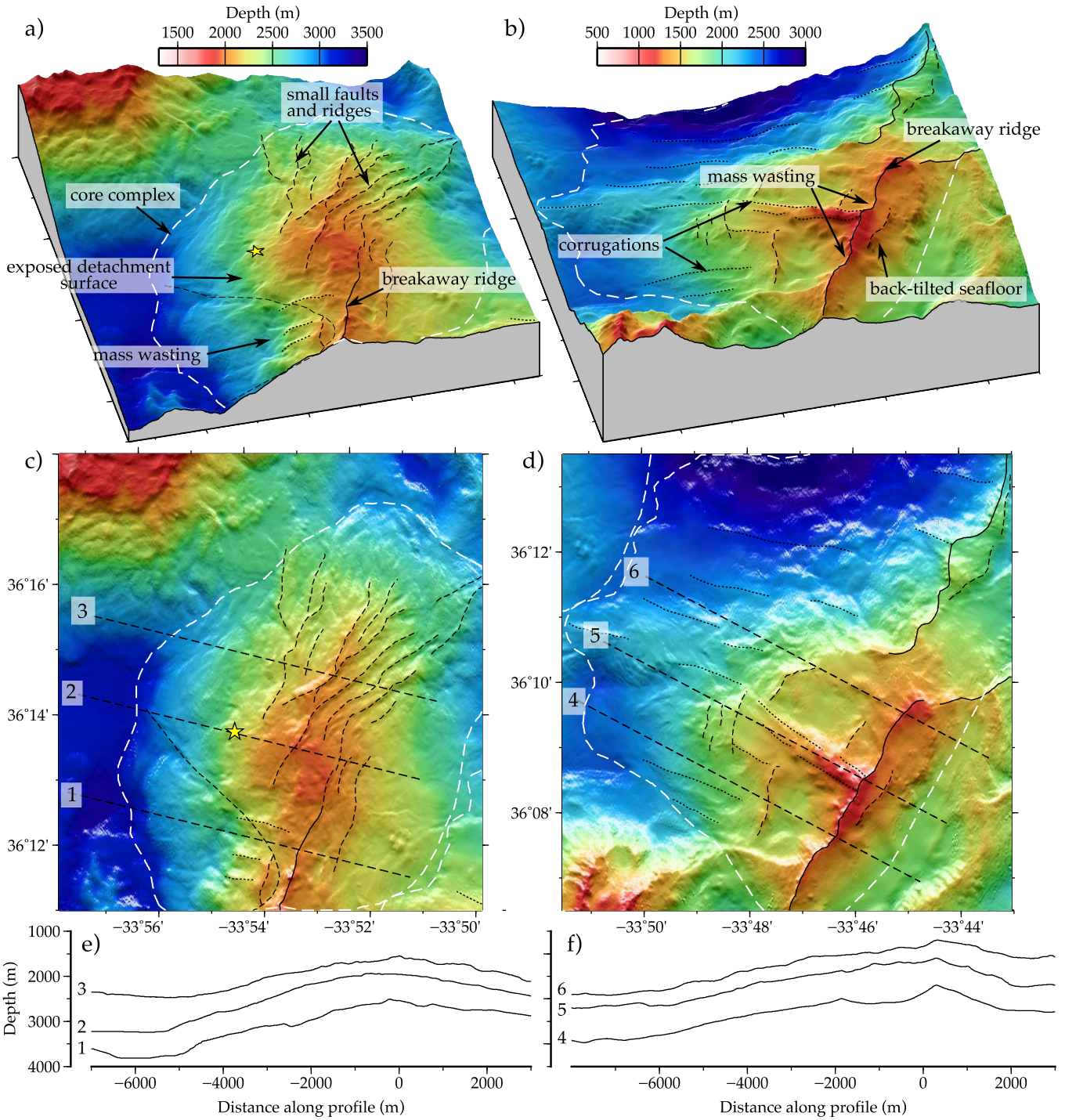

Figure 7. Detailed bathymetric maps of the Rainbow and Pot of Gold massifs/OCCs. (left) Rainbow massif; (right): Pot of Gold massif. (a, b) Three-dimensional isometric views. (c, d) Illuminated bathymetry and location of profiles shown in Figures 7e and 7f. The yellow star marks the location of the RHF. White dashed lines mark the extent of the OCCs, including the fossil detachment fault surfaces and back-tilted seafloor. (e, f) Cross sections through the OCCs showing the geometry of the flexural dome and back-tilted seabed.

perpendicular to the spreading direction, and the azimuth of the ridge axis (Figures 2c and 2d). This discrepancy suggests that the oblique component of spreading is not taken up entirely by the ridge offsets and that a small amount of shear deformation is distributed along the ridge segments.

The topography of the ridge flanks is elevated on the inside corners of the Rainbow NTD relative to the outside corners by up to 1500 m (Figure 1). Seabed depth decreases gradually along each ridge segment from

S to N on the east flank and from N to S on the west flank of the ridge. This general trend is complicated by the fact that some segments are very short and the effects of adjacent NTDs appear superimposed. The most prominent topographic highs are found ~20 km off-axis on the western flank of the AMAR Minor N segment and on the eastern flank of the S. AMAR segment, associated with large mode E faults (Figures 1b and 6a).

3.5. Tectonic Strain Estimate and Seafloor Domains

We used the observed distribution of exposed fault surface versus extrusive volcanic seafloor to derive a quantitative estimate of tectonic strain, *T*, and indirectly of the minimum magmatic accretion rate, *M*. The tectonic strain can be estimated as the fraction of seabed consisting of exposed fault surface along ridge-perpendicular profiles. Our approach is equivalent to method 3 of *Escartín et al*. [1999], i.e., we measure tectonic strain as the cumulative apparent fault heave along profiles divided by the profile's length. Uncertainties in our estimate arise from a number of factors, including sedimentation, the assumption that fault slip is parallel to the far-field extension, and ignoring the effects of mass wasting and talus accumulation. We restrict our profiles to within 16 km of the ridge axis in both directions (see example profiles in Figure 6b), to limit the uncertainty introduced by sedimentation masking the morphology away from the ridge. Mass wasting is likely to be the most significant source of error and may cause apparent heave to be larger than real heave by up to 67% for faults dipping at 60° [*Escartín et al*., 1999]. However, for large, shallow-dipping faults ($< 30°$), which are those that contribute the most to cumulative heave, the error is likely to be small.

The profiles are spaced every 200 m and allow us to estimate the variation of *T* along the ridge axis. It is important to note that we estimate the average tectonic strain over transects that correspond to the last ~1.5 Ma, and that actual tectonic strain may have varied considerably over this time period.

We find values of *T* mostly between 0.2 and 0.3 for the S. AMAR and AMAR segments and *T* ~0.4 for the AMAR Minor S and the AMAR Minor N segments. *T* increases rapidly at the Rainbow NTD where it reaches a value of 0.6–0.8. A low *T* (~0.2) is generally accompanied by smaller closely spaced faults while a large *T* is accompanied by larger wider-spaced faults (see e.g., Figure 6b, profiles 2 and 4). We also calculate *T* for the W and E flanks independently. *T* on the outside corners of the Rainbow NTD remains low, while it increases to almost 1.0 on the inside corners. The strongest tectonic strain asymmetry (across a ridge segment) is found just south of the Rainbow NTD.

Based on the distribution of faulting style, the occurrence of volcanic textures, the estimated tectonic strain and the gravity and magnetic expression we can identify three seafloor domains, similar to those defined by *Cannat et al* [2006]:

1. Volcanic seafloor is created by normal volcanic spreading and consists mostly of areas of extrusive volcanic morphology cut by regular closely spaced small-offset faults. It is found within the axial valley and on the ridge flanks near the centers of major segments, where the tectonic strain is low, usually associated with RMBA lows and strong magnetic anomalies.
2. Tectonized seafloor, equivalent to the smooth seafloor defined by *Cannat et al*. [2006], is created by nonvolcanic spreading [*Schroeder et al*., 2007] and consists of large smooth fossil detachment fault surfaces often intersected by smaller secondary faults. It is found in areas of very high tectonic strain, associated with RMBA highs and a subdued magnetic signature.
3. Hybrid volcanic/tectonized seafloor consists of areas of extrusive volcanic morphology displaced by large exposed fault surfaces forming widely spaced abyssal hills. It is generated by alternating volcanic/nonvolcanic spreading near segment ends and in areas of moderate tectonic strain, sometimes in association with axis parallel bands in RMBA and magnetization.

We do not find in this area any large corrugated surfaces corresponding to the corrugated seafloor described by *Cannat et al*. [2006]. The smooth nature of tectonized seabed is clearly displayed by comparing wavenumber spectra of bathymetry profiles drawn perpendicular to the ridge. The wavenumber power spectral density (PSD) of the profile crossing the Rainbow NTD shows a reduction in the short wavelength component and a lower corner wavenumber (Figure 6c), indicating a lack of short-wavelength bathymetric features.

4. Discussion

4.1. Crustal Accretion Along the Spreading Segments

The morphological and potential field observations provide two independent and complementary points of view to understand the tectonics of this section of the ridge and more in general the mechanisms driving nonvolcanic spreading.

The axial depth, the style of extrusive volcanism and the style of faulting vary systematically along the ridge segments and are consistent with the observed RMBA and magnetization. We find a positive correlation of *T* with RMBA (Figure 6d). In addition the RMBA (Figure 4a) shows a similar pattern to the seabed fabric alignment map (Figure 2d): RMBA highs correspond to areas that lack seafloor fabric alignment (high standard deviation of lineament strike), while RMBA lows correspond to strongly lineated terrain. This correspondence suggests that faulting style and crustal thickness at slow spreading ridges are strongly linked. The relationship is likely to be indirect and to be controlled by the style of crustal accretion at the ridge. If we assume that the observed variation in RMBA is primarily due to crustal thickness variations (higher RMBA = thinner crust) we can deduce an inverse relationship between tectonic strain and crustal thickness. Making the additional assumption that crustal thickness is mainly controlled by magmatic input, our observations imply that in this area an increase in tectonic strain is accompanied by an equivalent reduction in total magmatic input and suggest that magmatic input into the footwall may be low (M_{FW} close to zero). A high rate of magmatic accretion and a low tectonic strain result in a thick, layered crust and regular closely spaced faults, which produce a strongly lineated terrain. Conversely a low rate of magmatic accretion and high tectonic strain result in a thin crust stretched by the action of large detachment faults, which produce an irregular "amorphous" seabed lacking clear lineations.

Assuming a simple reciprocal relationship between magmatic accretion rate and tectonic strain ($M=1-T$), our *T* estimate indicates that the magmatic input is relatively high on the S. AMAR and AMAR segments, slightly lower on the AMAR Minor S and the AMAR Minor N segments, and very low at the Rainbow NTD. Similarly, the RMBA shows prominent lows on the centers of the AMAR and S. AMAR segments, indicating a relatively thick igneous crust, and a weaker low on the AMAR Minor S segment but not on the AMAR Minor N segment. We deduce that magmatic input is focused at segment centers and that the AMAR and S. AMAR, and to a lesser extent the AMAR Minor S, segments are the main accretionary segments, while the AMAR Minor N segment is lower order and possibly represents a morphological, but not mantle-level, segmentation.

4.2. Accretion Asymmetry

The Rainbow NTD is associated with a strong inside corner/outside corner topographic asymmetry, which is accompanied by an asymmetry in magmatic accretion rate and faulting style. The highest topography and strongest RMBA are found at inside corners and are associated with increased tectonic strain. Inside corner/outside corner topographic asymmetry is a common feature of transform and nontransform discontinuities on slow-spreading ridges [e.g., *Severinghaus and Macdonald*, 1988; *Tucholke and Lin*, 1994; *Thibaud et al*., 1998]. Several models have been proposed to explain inside corner topographic highs, including coupling of young and old lithosphere across the discontinuity [*Severinghaus and Macdonald*, 1988], dynamic topography sustained by a twisting moment resulting from depth-dependent stress across the shear zone [*Chen*, 1989], the effect of viscoelastic shear deformation [*Bercovici et al*., 1992], serpentinization-driven buoyancy [*Bonatti*, 1976], and flexural uplift induced by detachment faulting [*Lavier et al*., 1999].

Numerical modeling of detachment faults in an elastic-plastic plate [*Lavier et al*., 1999] indicates that the largest footwall block uplift is expected when cumulative slip on the fault is a few km (comparable to plate thickness) since in this case the initial fault breakaway is superimposed on the flexural bulge. If slip continues further, regional isostatic compensation causes bending of the fault surface and flattening of the flexural bulge [*Buck,* 1988]. Accordingly, the highest inside corner topography at Rainbow is associated with mode E faults, which have cumulative slip of 3–4 km, rather than the fully developed detachment faults. It seems likely that repeated development of mode E faults and detachment faults on the inside corners of ridge offsets is an important factor in generating inside corner topographic highs, however detailed three-dimensional modeling is needed to determine the relative importance of all proposed mechanisms. *Behn et al*. [2002] showed that the development of mode E faults at inside corners may be explained by weakening of the lithosphere at segment ends due to serpentinization or by shear stresses acting across the offset.

Both mechanisms are likely at play at Rainbow. Fault strike azimuths near the Rainbow NTD are rotated clockwise by up to 45° (Figure 6a), which would indicate that high shear stresses are sustained across the offset [*Grindlay and Fox*, 1993]. However, a significant component of the inferred stress rotation may be due to extension driven by local topographic imbalance [e.g., *Neves et al*., 2004].

On the S. AMAR and AMAR Minor S segments an alternation of large faults and volcanic seafloor (Figure 6a) is associated with alternating areas of high and low topography (Figure 1b) and with axis-parallel bands of alternating high/low magnetization and RMBA (Figure 4) with width of 4–5 km. The bands likely correspond to individual fault blocks uplifted and tilted by associated mode E faults. The back-tilted seafloor shows volcanic morphology, strong magnetization and low RMBA, indicating a magmatic origin (Figures 4, 5b, and 6b). The exposed fault surfaces are associated with low magnetization and relatively high RMBA indicating crustal thinning and exhumation of less magnetic lower crustal and mantle rocks. A pattern of alternating volcanic/nonvolcanic spreading may be explained by temporal variations in the partitioning of magmatic accretion and tectonic strain between conjugate flanks caused by alternating nucleation of large mode E faults on the opposite flanks of the axial valley [*Cannat et al*., 2006].

In the latter scenario the total magmatic input could remain stable or only change gradually over a long time scale, while the accretion asymmetry changes more rapidly. Age constraints from the magnetization inversion suggest that mode E faulting has alternated between the E and W flank and support this interpretation (Figures 4 and 6). Because of the short length of the AMAR Minor S segment, mode E faults affect the whole segment and not just the segment ends. This implies that mode E faults associated with the Rainbow NTD may be in competition with those associated with the S. AMAR NTD. This competition may provide a mechanism for flip-flopping of faulting between the conjugate valley flanks. Alternatively this behavior may arise from simple kinematic constraints imposed by the balance between magmatic accretion and tectonic strain. Numerical models predict a similar behavior when M is $\sim$0.7 [*Behn and Ito*, 2008; *Tucholke et al*., 2008], close to our estimate of 0.6 for the AMAR Minor S segment.

Strong asymmetry in both the style and rate of accretion is evident from the seabed magnetization map. In particular, we observe variations in the width of the Matuyama magnetic chron on the AMAR segment (grey arrows in Figure 4b), indicating about two times faster spreading on the west compared to the east flank. This asymmetry suggests that the ridge axis of the AMAR segment may have moved to the east compared to the AMAR Minor N segment, creating the AMAR NTD. We also note that at the segment ends near the Rainbow NTD the Brunhes/Matuyama reversal is $\sim$5 km off-axis on the outside corners and $\sim$15 km off-axis on the inside corners (green arrows, Figure 4b), suggesting a 75%–25% partitioning of accretion between the inside and outside corners respectively. If this asymmetry were sustained for a long period of time it would cause the ridge axis to migrate toward the outside corners, widening the Rainbow NTD, as inferred for example on the Southwest Indian Ridge near Atlantis Bank [*Baines et al*., 2007*; John and Cheadle*, 2010]. With a total spreading rate of 22 mm/yr it would have taken just over 1 Myrs to generate the 12 km offset presently attained by the Rainbow NTD. This interpretation is based on the assumption that plate spreading is focused entirely on the ridge axis and that the ridge is continuous in time, i.e., it does not jump laterally. We know, however, that extension at slow spreading ridges can affect the whole axial valley and that during detachment faulting a large percentage of plate separation can become localized on a single fault on the valley wall [e.g., *Grimes et al*., 2008, *MacLeod et al*., 2009]. In addition, the two nodal basins on either side of the Rainbow massif are filled with sediments, indicating suppressed volcanism. In this case it may not be meaningful to associate zero age with the volcanic ridge axis and to calculate average spreading rates by measuring the distance between the Brunhes/Matuyama reversal and the ridge axis. We suggest that at least part of the observed plate age asymmetry is due to the fact that the center of plate separation at segment ends does not correspond with the middle of the axial valley and the maximum in magnetic anomaly, which were used to trace the ridge axis, but is instead located on the inside corner valley wall. Based on the seabed morphology and shape of magnetic reversals the Rainbow NTD likely developed over at least the last 3.5 Myr.

We notice a $\sim$5 mGal higher RMBA on the east flank compared to the west flank of the S. AMAR and AMAR Minor S segments which may indicate long-term asymmetric magmatic emplacement and crustal thickness or a skewed mantle thermal structure, perhaps due to relative motion of the plate boundary with respect to the asthenosphere.

4.3. Temporal Variability of Accretion Style

The off-axis trace of the Rainbow NTD forms a V-shaped wake visible in the bathymetry, gravity and magnetization maps (Figures 2–4) indicating a long history of low magma supply and nonvolcanic spreading. The wake itself is asymmetric since it is the result of inside corner/outside corner topography variations and consists of topographic highs extending from the inside corners and parallel depressions extending from the outside corners. The wake comprises the highly tectonized seafloor of the NTD, the off-axis Pot of Gold and Clurichaun massifs/OCCs, and the series of heavily sedimented basins that extend to the ENE and NNW (Figure 1b). The limits between segments (white dashed lines in Figure 4) were picked between the inside corner highs and outside corner basins, based on the RMBA and bathymetry, as well as the location of the kink in the fault traces and the magnetic isochrons.

The internal angle of the wake is ~120° suggesting southward migration at ~6 mm/yr, or about a quarter of the spreading rate. Similar patterns have been observed by *Morris and Detrick* [1991] and by *Rommevaux et al*. [1994] on other sections of the MAR. NTD migration has been described in the past but is not well understood [e.g., *Schouten et al*., 1987; *Gente et al*., 1995; *Detrick et al*., 1995; *Thibaud et al*., 1998; *Rabain et al*., 2001; *Searle and Escartín*, 2004]. The migration of the NTD may be driven by temporal changes in magmatic input on the ridge segments, perhaps caused by instabilities in secondary mantle convection [*Rouzo et al*., 1995] or related to motion of the plate boundary with respect to the asthenospheric flow [*Katz et al*., 2004]. The southward migration of the Rainbow NTD implies a lengthening of the magmatically strong AMAR segment and a shortening of the magmatically weak AMAR Minor S segment by ~20 km in the last 2–3 Myr. However the southward migration seems to have slowed in the last 1 Myr, perhaps in conjunction with a weakening of the magmatic input and emergence of the AMAR Minor N segment.

The S. AMAR NTD is associated with a disruption in faulting which can be followed off-axis to lithospheric ages of ~2 Myr. The seabed morphology and the *T* estimate do not indicate a significant reduction in magmatic input, however the RMBA indicates crustal thinning in this region. The AMAR NTD is also associated with disrupted faulting and low magnetization, suggesting significant magmatic input disruption. The short off-axis trace indicates that it is a recent feature. Both may be classified as third order or Type 3 offsets [*Grindlay et al*., 1991*; Spencer et al*., 1997], i.e., small offsets that are not associated with major shear deformation structures. They give rise to some mode E faults on the inside corners, but these do not develop into very large detachment faults.

4.4. Crustal Accretion at Rainbow

The Rainbow massif is characterized by many of the features typical of OCCs, i.e., the dome shape, the smooth seafloor texture, the presence of a sharp slope break between the massif's flank and the nodal basin to the west and exposures of lower crustal and mantle rocks. We show that the western flank of the massif is associated with a local RMBA high and weak magnetization, indicating more pronounced crustal thinning and mantle exhumation in this area, as would be expected near the hanging wall cutoff of a detachment fault. In addition, asymmetric morphology and plate ages (inferred from the seabed magnetization map) suggest that tectonic strain has been focused on the massif's western flank. Together, these observations strongly support the interpretation of the western flank as the exposed portion of the detachment fault responsible for uplifting the massif [*Andreani et al*., 2014].

Our magnetic data show that plate spreading was strongly asymmetric at Rainbow at least over the last 1 Myr (section 4.2), with a large percentage of plate separation focused on the inside corner, suggesting that the hanging wall cut-off has migrated westward toward and across the ridge axis. This may have resulted in magma injection and emplacement of gabbro bodies within the OCC, which could lead to the detachment fault becoming inactive [e.g., *MacLeod et al*., 2009]. Dredge samples show that sediments cover the lower part of the massif and indicate that the detachment fault may in fact be already inactive [*Andreani et al*., 2014]. The Rainbow detachment and previous detachment faults formed at the Rainbow NTD lack substantial corrugations, which are often observed at other OCCs [e.g., *Smith et al*., 2006]. Although the origin of OCC corrugations is unclear, one hypothesis is that they are formed at an irregular brittle-plastic transition depth due to intrusion of magma into the footwall [*Tucholke et al*., 2008]. Under this hypothesis the lack of substantial corrugations at Rainbow may be due to a brittle-plastic transition that is not stable at depth during the lifetime of OCC formation, or alternatively may be the result of extensive mass wasting degrading the detachment fault surface after it is exposed.

The eastern flank of the massif is characterized by stronger magnetization and relatively lower RMBA (Figure 4) and may be interpreted as the original seafloor, which was back-tilted by the action of the detachment fault (Figure 7). A scarp on the southern end of the massif, where the composition of recovered dredges and the seabed morphology show that the preexisting crust had a volcanic top layer, could be interpreted as a breakaway ridge. In the northern part of the massif this breakaway ridge is not preserved, perhaps due to subsequent faulting or a weaker rheology.

We observe a set of SW-NE trending faults on the summit of the Rainbow massif, which has been previously described by *Andreani et al*. [2014]. These faults seem to link with a set of curved faults and volcanic ridges in the nodal basin east of Rainbow and may correspond to second-generation faults formed after the main detachment fault was abandoned. Alternatively they may be contemporaneous to detachment faulting and may represent a zone of diffuse deformation accommodating extension and shear strain on the nontransform discontinuity. The slip mechanism is unclear from the morphology, however they are likely to involve normal and strike-slip displacement. Numerical modeling [*Tucholke et al*., 2008] and observations of microearthquake hypocenters from the TAG hydrothermal site [*deMartin et al*., 2007] show that second-generation faults can reach deep into the lithosphere and could enhance permeability in the footwall of the detachment fault, facilitating hydrothermal fluid flow, chemical alteration and heat extraction. Other factors that may contribute to deformation and fracturing of the massif include extensional bend faulting caused by flexure of the detachment fault footwall or local stresses induced by serpentinite diapirism or by gravity-driven lateral collapse of the massif facilitated by the presence of mechanically weak serpentinite.

We observe extensive fault linkage throughout the survey area, and in particular in areas of high tectonic strain, as often observed in continental rift settings and other extensional environments [e.g., *Crider and Pollard*, 1998; *Bose and Mitra*, 2009]. For example, we note that faults are intricately linked on the western flank of the AMAR Minor S segment and that the Rainbow OCC and the Pot of Gold OCC are both linked to the south with mode E faults (Figure 6a). The valley walls seem to form an almost continuous interconnected system of faults extending over the whole ridge section, reminiscent of the model of a laterally continuous detachment proposed by *Reston and Ranero* [2011]. The fault systems seem continuous across the two smaller NTDs and even across the western flank of the Rainbow NTD. Given the general clockwise rotation of the ridge with respect to the direction perpendicular to the far field extension, linkage of adjacent faults is mostly accomplished via right-stepping relays or step-overs. In this interpretation the Rainbow massif can be thought of as a large right-stepping relay structure on the eastern axial valley wall.

It is interesting to note that an inventory of geothermal systems in the extensional Great Basin region in the western USA [*Faulds et al*., 2011*; Faulds and Hinz*, 2015] found that step-overs and relay ramps are the most favorable settings for geothermal systems in that region, because such areas are characterized by increased fracture density and permeability. A similar mechanism may be at play at Rainbow and other similar hydrothermal systems located on the axial valley walls near NTDs or on smaller relay zones (e.g., Logatchev, Ashadze [*Smith et al*., 2008] and Saldanha [*Gràcia et al*., 2000]).

4.5. Implications for the Heat Source Driving the RHF

Recent migration over the ridge axis of the hanging wall cut-off of the Rainbow detachment fault may have provided a mechanism for input of magma into the footwall [*MacLeod et al*., 2009] despite the low magmatic input at the NTD. A crystallizing magma body remains therefore a likely candidate for the primary heat source of the RHF. It may be generated *in situ* by decompression melting due to footwall exhumation during detachment faulting as suggested by *Canales et al*. [2008], or it may be emplaced vertically from a deeper source arising from mantle temperature anomalies or other transient conditions in the mantle. Alternatively it may be emplaced laterally from the adjacent ridge segments by dykes propagating along the ridge axis [e.g., *Grandin et al*., 2012]. It remains to be explained why surface volcanism is almost completely suppressed. Numerical modeling of dyke propagation [*Maccaferri et al*., 2014] shows that on continental rift zones certain thermal and structural conditions can lead to the development of stress barriers that inhibit magma ascent, favoring instead magma intrusion and suppressing surface volcanism.

Other more speculative hypotheses for the heat source of the RHF involve a more central role of detachment faulting, fracture networks and chemical alteration of ultramafic rocks. *Behn and Ito* [2008] show that significant temperature anomalies can develop beneath the footwalls of detachment faults at the base of the lithosphere. In addition we showed that the Rainbow massif is likely to be a region of increased faulting

and fracturing. Increased temperatures and heat flux due to prolonged footwall uplift and increased permeability associated with extensive fracturing are likely to play an important role in sustaining high-temperature fluid circulation.

5. Conclusions

We present new multibeam bathymetry and potential field data from the MAR between 35°40′N and 36°40′N. We mapped faulting style, seabed characteristics, RMBA (which can be used as a proxy for crustal thickness) and seabed magnetization along this section of the ridge. The observed spatial variations can be explained by temporal and spatial changes in the style of accretion, which we parameterize by the tectonic strain, *T*, and the magmatic accretion rate, *M*.

Faulting style varies with the tectonic strain, *T*, as predicted by numerical models. We find regular closely-spaced bookshelf style faults on sections of the ridge with $T = 0.2$-0.3 and larger wider-spaced shallow-dipping faults on sections of the ridge where *T* approaches 0.5. At the Rainbow NTD we find *T* in the range 0.6-0.8, in conjunction with high RMBA and a strongly tectonized terrain similar to the smooth seafloor described by *Cannat et al*. [2006] on the Southwest Indian Ridge and indicative of extensive mantle exhumation. In general we find a strinkingly close correspondence between RMBA, seabed morphology and tectonic strain, suggesting a close control of magmatic input on faulting style and crustal thickness.

We calculate *T* on the conjugate sides of the axial valley and show that asymmetric topography and faulting style at offset corners is accompanied by an asymmetry in magmatic accretion and tectonic strain. At inside corners the tectonic strain increases to almost 1.0, but it remains below 0.5 on the conjugate outside corners. Asymmetric magnetic chrons indicate asymmetric accretion rate at the inside corners of the Rainbow NTD (75%-25% accretion partitioning between inside and outside corners), which may have caused widening of the NTD since the Bruhnes/Matuyama reversal (0.78 Ma). However, we argue that at least part of the plate age asymmetry may be apparent and may be caused by focusing of more than half of the plate separation on single long-lived faults on the valley walls at inside corners. There is also a marked topographic asymmetry between the inside corners and the outside corners of the Rainbow NTD, which originates at the valley walls. We suggest that the asymmetry in accretion style and rate and preferential nucleation of mode E faults and detachment faults at inside corners play a major role in generating inside corner highs.

Alternating bands of high/low magnetization and RMBA associated with large mode E faults indicate alternating volcanic accretion and tectonic denudation over a $\sim$1 Myr timescale and flip-flopping of mode E fault nucleation between the conjugate sides of the AMAR Minor S segment, which may be driven by stress interaction between closely spaced NTDs.

The magmatic input has varied over different time scales as evidenced by changes in fault size and spacing away from the ridge, contrasting OCC morphologies, and the oblique NTD trace. The V-shaped wake of the Rainbow NTD suggests that the segment to the north (the AMAR segment and more recently the AMAR Minor N segment) has been growing at the expense of the segment to the south (the AMAR Minor S segment) for at least the last 3.5 Myr. However, this trend may have slowed in the last 1 Myr, accompanied by a weakening of magmatic input in the southern part of the AMAR segment and the emergence of the AMAR Minor N subsegment. These observations support the idea that the location and evolution of second order segmentation of the ridge may be determined by heterogeneities in the temperature and/or chemical structure of the upper mantle perhaps related to secondary mantle convection.

We identified a number of detachment faults associated with the Rainbow NTD, including one composing the western flank of the Rainbow massif and at least two on the off-axis trace of the NTD (The Pot of Gold massif and the Clurichaun massif). We report extensive fault linking throughout the survey area, and in particular linking between detachment faults and adjacent mode E faults, supporting the model of a laterally continuous detachment fault proposed by *MacLeod et al*. [2009].

OCCs generated at Rainbow lack clear corrugations and seem disrupted by second generation faults. We suggest that OCC formation at NTDs is affected by the perturbed stress regime and by temporal and spatial variations in tectonic strain. The observed high tectonic strain and plate age asymmetry at Rainbow imply that the detachment fault has migrated toward the ridge axis. This may have caused a recent increase in

magmatic input into the footwall and may be responsible for stopping detachment faulting on the massif's western flank and driving hydrothermal activity at the RHF.

Outward dipping faults outcropping near the summit of the Rainbow massif may represent a zone of diffuse deformation, accomodating extension and shear strain on the NTD or may correspond to second-generation faults which accomodate deformation after the main detachment is abandoned. Other factors contributing to fracturing of the massif may include footwall flexure, gravitational collapse and stresses induced by serpentinization. In any case fracturing of the massif and deep penetrating faults likely increase permeability and facilitate fluid flow and heat extraction.

We propose a crustal accretion model for the Rainbow area similar to scenario (b) of *Olive et al*. [2010], which involves the emplacement of isolated gabbro intrusions in the middle and lower crust and their exhumation by detachment faulting together with serpentinized mantle peridotites. The most likely mechanism for the heat source driving hydrothermal activity at the RHF is a solidifying magma body emplaced within the footwall of the detachment fault forming the western flank of the Rainbow massif. Other important factors likely include a long-lived thermal anomaly associated with detachment faulting and enhanced heat flow and permeability due to footwall upwelling and fracturing. By inference, a similar combination of detachment fault migration toward the ridge axis, capture of magmatic input into the footwall and increased fracturing and permeability may be at play at other OCC-hosted high-temperature hydrothermal systems, e.g., Logatchev and Ashadze.

Acknowledgments

We are grateful to the captain and crew of the *R/V M. G. Langseth* for their support during the MGL1305 expedition and to all other participants to the field campaign for their help at sea. We thank Y. Fouquet and B. Loubrieu from IFREMER Marine Geosciences Department for granting us access to the FLORES cruise swath bathymetry data. Our analysis and interpretation benefited from fruitful discussion with M. Behn, B. Tucholke and M. Tivey. The stimulating and constructive comments of T. Reston and two other anonimous reviewers and of the associate editor M. Cheadle helped us improve the paper. The experiment was funded by NSF grants OCE-0961151 (RAD) and OCE-0961680 (JPC). The data are available from the Marine Geoscience Data System database. M. Paulatto was supported by an InterRidge cruise bursary, an InterRidge postdoctoral fellowship and an AXA postdoctoral fellowship. Figures were prepared with the *Generic Mapping Tools* [*Wessel et al*., 2013] and edited in *Inkscape* [https://inkscape.org].

References

Allen, D. E., and W. E. Seyfried Jr. (2004), Serpentinization and heat generation: Constraints from Lost City and Rainbow hydrothermal systems, *Geochim. Cosmochim. Acta*., *68*(6), 1347–1354, doi:10.1016/j.gca.2003.09.003.

Andreani, M., J. Escartín, A. Delacour, B. Ildefonse, M. Godard, J. Dyment, and Y. Fouquet (2014), Tectonic structure, lithology, and hydrothermal signature of the Rainbow massif (Mid-Atlantic Ridge 36°14′N), *Geochem. Geophys. Geosyst*., *15*, 3543–3571, doi:10.1002/2014GC005269.

Baines, A. G., M. J. Cheadle, H. J. Dick, A. H. Scheirer, B. E. John, N. J. Kusznir, and T. Matsumoto (2007), Evolution of the Southwest Indian Ridge from 55°45′ E to 62°E: Changes in plate-boundary geometry since 26 Ma, *Geochem. Geophys. Geosyst*., *8*, Q06022, doi:10.1029/2006GC001559.

Behn, M. D., and G. Ito (2008), Magmatic and tectonic extension at mid-ocean ridges: 1. Controls on fault characteristics, *Geochem. Geophys. Geosyst*., *9*, Q08O10, doi:10.1029/2008GC001965.

Behn, M. D., J. Lin, and M. T. Zuber (2002), Mechanisms of normal fault development at mid-ocean ridges, *J. Geophys. Res*., *107*(B4), 2083, doi:10.1029/2001JB000503.

Bercovici, D., H. J. Dick, and T. P. Wagner (1992), Nonlinear viscoelasticity and the formation of transverse ridges, *J. Geophys. Res*., *97*, 14,195–14,206, doi:10.1029/92JB00890.

Bonatti, E. (1976), Serpentinite protrusions in the oceanic crust, *Earth Planet. Sci. Lett*., *32*(2), 107–113, doi:10.1016/0012–821X(76)90048-0.

Bose, S., and Mitra, S. (2009), Deformation along oblique and lateral ramps in listric normal faults: Insights from experimental models, *AAPG Bull*., *93*(4), 431–451, doi:10.1306/12080808117.

Buck, W. R. (1988), Flexural rotation of normal faults, *Tectonics*, *7*, 959–973, doi:10.1029/TC007i005p00959.

Buck, W. R., L. L. Lavier, and A. N. B. Poliakov (2005), Modes of faulting at mid-ocean ridges, *Nature*, *434*, 719–723, doi:10.1038/nature03358.

Canales, J. P., R. S. Detrick, J. Lin, J. A. Collins, and D. R. Toomey (2000), Crustal and upper mantle seismic structure beneath the rift mountains and across a nontransform offset at the Mid-Atlantic Ridge (35°N), *J. Geophys. Res*., *105*, 2699–2719, doi:10.1029/1999JB900379.

Canales, J. P., B. E. Tucholke, M. Xu, J. A. Collins, and D. L. DuBois (2008), Seismic evidence for large-scale compositional heterogeneity of oceanic core complexes, *Geochem. Geophys. Geosyst*., *9*, Q08002, doi:10.1029/2008GC002009.

Canales, J. P., et al. (2013), MARINER: Seismic Investigation of the Rainbow Hydrothermal Field and its Tectono/Magmatic Setting, Mid-Atlantic Ridge 36° 14′N—A Report from RV M.G. Langseth Cruise MGL1305, *InterRidge News*, *22*, 46–52.

Canny, J. (1986), A Computational approach to edge detection, *IEEE Trans. Pattern Anal*., *6*, 679–698, doi:10.1109/TPAMI.1986.4767851.

Cann, J. R. (1974), A model for oceanic crustal structure developed, *Geophys. J. R. Astron. Soc*., *39*, 169–187, doi:10.1111/j.1365-246X.1974.tb05446.

Cann, J. R., and M. R. Strens (1982), Black smokers fuelled by freezing magma, *Nature*, *298*, 147–149, doi:10.1038/298147a0.

Cannat, M. (1996), How thick is the magmatic crust at slow spreading oceanic ridges, *J. Geophys. Res*., *101*, 2847–2857.

Cannat, M., C. Mevel, M. Maia, C. Deplus, C. Durand, P. Gente and J.Reynolds (1995), Thin crust, ultramafic exposures, and rugged faulting patterns at the Mid-Atlantic Ridge (22–24°N), *Geology*, *23*(1), 49–52.

Cannat, M., A. Briais, C. Deplus, J. Escartín, J. Georgen, J. Lin, and P. da Silva (1999), Mid-Atlantic Ridge–Azores hotspot interactions: Along-axis migration of a hotspot-derived event of enhanced magmatism 10 to 4 Ma ago, *Earth Planet. Sci. Lett*., *173*(3), 257–269.

Cannat, M., D., Sauter, V. Mendel, E. Ruellan, K. Okino, J. Escartín, and M. Baala (2006), Modes of seafloor generation at a melt-poor ultra-slow-spreading ridge, *Geology*, *34*(7), 605–608.

Cave, R. R., C. R. German, J. Thomson, and R. W. Nesbitt (2002), Fluxes to sediments underlying the Rainbow hydrothermal plume at 36°14′ N on the Mid-Atlantic Ridge, *Geochim. Cosmochim. Acta*, *66*(11), 1905–1923, doi:10.1016/S0016–7037(02)00823-2.

Charlou, J. L., J. P. Donval, Y. Fouquet, P. Jean-Baptiste, and N. Holm (2002), Geochemistry of high H2 and CH4 vent fluids issuing from ultramafic rocks at the Rainbow hydrothermal field (36° 14′ N, MAR), *Chem. Geol*., *191*(4), 345–359, doi:10.1016/S0009–2541(02)00134-1.

Chen, Y. (1989), A mechanical model for the inside corner uplift at a ridge-transform intersection, *J. Geophys. Res*., *94*, 9275–9282, doi:10.1029/JB094iB07p09275.

Colman, A., J. M. Sinton, S. M. White, J. T. McClinton, J. A. Bowles, K. H. Rubin, and C. Russo (2012), Effects of variable magma supply on mid-ocean ridge eruptions: Constraints from mapped lava flow fields along the Galápagos Spreading Center, *Geochem. Geophys. Geosyst*., *13*, Q08014, doi:10.1029/2012GC004163.

Crider, J. G., and D. D. Pollard (1998), Fault linkage: Three-dimensional mechanical interaction between echelon normal faults, *J. Geophys. Res*, *103*, 24,373–24,391, doi:10.1029/98JB01353.

deMartin, B. J., R. A. Sohn, J. P. Canales, and S. E. Humphris (2007), Kinematics and geometry of active detachment faulting beneath the Trans-Atlantic Geotraverse (TAG) hydrothermal field on the Mid-Atlantic Ridge, *Geology*, *35*(8), 711–714, doi:10.1130/G23718A.1.

DeMets, C., R. G. Gordon, and D. F. Argus (2010), Geologically current plate motions, *Geophys. J. Int.*, *181*(1), 1–80, doi:10.1111/j.1365-246X.2009.04491.x.

Detrick, R. S., H. D. Needham, and V. Renard (1995), Gravity anomalies and crustal thickness variations along the Mid-Atlantic Ridge between 33°N and 40°N, *J. Geophys. Res.*, *100*, 3767–3787, doi:10.1029/94JB02649.

Dick, H. J., J. H. Natland, J. C. Alt, W. Bach, D. Bideau, J. S. Gee, and A. Yoshinobu (2000), A long in situ section of the lower ocean crust: Results of ODP Leg 176 drilling at the Southwest Indian Ridge, *Earth Planet. Sci. Lett.*, *179*(1), 31–51.

Dick, H. J., M. A. Tivey and B. E. Tucholke (2008), Plutonic foundation of a slow-spreading ridge segment: Oceanic core complex at Kane Megamullion, 23°30′ N, 45°20′ W, *Geochem. Geophys. Geosys.*, *9*(5), doi:10.1029/2007GC001645.

Dunn, R., J. P. Canales, R. Sohn, R. Arai, and M. Paulatto (2014), Melt supply, crustal structure, tectonic rifting, and hydrothermal venting at the rainbow area, 36° N MAR, in *EGU General Assembly Conference Abstracts*, Vienna, Austria., vol. 16, pp. 12092.

Dunn, R. A., J. P. Canales, R. A. Sohn, M. Paulatto, R. Arai, and F. Szitkar (2013), The MARINER Integrated Seismic and Geophysical Mapping Experiment, Abstract T21F-07 presented at 2013 Fall Meeting, AGU, San Francisco, Calif.

Escartín, J., P. A. Cowie, R. C. Searle, S. Allerton, N. C. Mitchell, C. J. MacLeod, and A. P. Slootweg (1999), Quantifying tectonic strain and magmatic accretion at a slow spreading ridge segment, Mid-Atlantic Ridge, 29 N, *J. Geophys Res.*, *104*, 10,421–10,437, doi:10.1029/1998JB900097.

Faulds, J. E., and N. H. Hinz (2015), Favorable tectonic and structural settings of geothermal systems in the Great Basin Region, Western USA: Proxies for discovering blind geothermal systems, paper presented at World Geothermal Congress 2015, Geothermal Resources Council annual meeting 2011, 23–26 October, San Diego, Calif.

Faulds, J. E., M. F. Coolbaugh, N. H. Hinz, P. H. Cashman, C. Kratt, G. Dering, J. Edwards, B. Mayhew, and H. McLachlan (2011), Assessment of favorable structural settings of geothermal systems in the Great Basin, western USA, *Trans. Geotherm. Resour. Counc.*, *35*, 777–784.

Fouquet, Y., J. L. Charlou, H. Ondreas, J. Radford-Knoery, J. P. Donval, E. Douville, and A. Ribeiro (1997), Discovery and first submersible investigations on the Rainbow hydrothermal field on the MAR (36 14′ N), *Eos Trans. AGU*, *78*(46), F832.

Gee, J. S., and D. V. Kent (2007), Source of oceanic magnetic anomalies and the geomagnetic polarity time scale, in *Treatise on Geophysics, Vol. 5: Geomagnetism*, edited by G. Schubert, Elsevier, Amsterdam, pp. 455–507, doi:10.1016/B978-044452748-6.00097-3.

Gente, P., R. A. Pockalny, C. Durand, C. Deplus, M. Maia, G. Ceuleneer, C. Mével, M. Cannat, and C. Laverne (1995), Characteristics and evolution of the segmentation of the Mid-Atlantic Ridge between 20°N and 24°N during the last 10 million years, *Earth Planet. Sci. Lett.*, *129* (1–4), 55–71, doi:10.1016/0012-821X(94)00233-O.

Georgen, J. E., J. Lin, and H. J. Dick (2001), Evidence from gravity anomalies for interactions of the Marion and Bouvet hotspots with the Southwest Indian Ridge: Effects of transform offsets, *Earth Planet. Sci. Lett.*, *187*(3), 283–300, doi:10.1016/S0012-821X(01)00293-X.

German, C. R., G. P. Klinkhammer, and M. D. Rudnicki (1996), The Rainbow hydrothermal plume, 36°15′ N, MAR, *Geophys. Res. Lett.*, *23*, 2979–2982, doi:10.1029/96GL02883.

German, C. R., A. M. Thurnherr, J. Knoery, J. L. Charlou, P. Jean-Baptiste, and H. N. Edmonds (2010), Heat, volume and chemical fluxes from submarine venting: A synthesis of results from the Rainbow hydrothermal field, 36°N MAR, *Deep Sea Res., Part I*, *57*(4), 518–527, doi: 10.1016/j.dsr.2009.12.011.

Gràcia, E., J. L. Charlou, J. Radford-Knoery, and L. M. Parson (2000), Non-transform offsets along the Mid-Atlantic Ridge south of the Azores (38°N–34°N): Ultramafic exposures and hosting of hydrothermal vents, *Earth Planet. Sci. Lett.*, *177*(1), 89–103, doi:10.1016/S0012-821X(00)00034-0.

Grandin, R., A. Socquet, C. Doubre, E. Jacques, and G. C. P. King (2012), Elastic thickness control of lateral dyke intrusion at mid-ocean ridges, *Earth Planet. Sci. Lett.*, *319–320*, 83–95, doi:10.1016/j.epsl.2011.12.011.

Grimes, C. B., B. E. John, M. J. Cheadle, and J. L. Wooden (2008), Protracted construction of gabbroic crust at a slow spreading ridge: Constraints from 206Pb/238U zircon ages from Atlantis Massif and IODP Hole U1309D (30°N, MAR), *Geochem. Geophys. Geosyst. 9*, Q08012, doi:10.1029/2008GC002063.

Grindlay, N. R., and P. J. Fox (1993), Lithospheric stresses associated with non-transform offsets of the Mid-Atlantic Ridge: Implications from a finite element analysis, *Tectonics*, *12*, 982–1003, doi:10.1029/93TC00364.

Grindlay, N. R., P. J. Fox, and K. C. Macdonald (1991), Second-order ridge axis discontinuities in the south Atlantic: Morphology, structure, and evolution, *Mar. Geophys. Res.*, *13*(1), 21–49, doi:10.1007/BF02428194.

Hooft, E. E. E., R. S. Detrick, D. R. Toomey, J. A. Collins, and J. Lin (2000), Crustal thickness and structure along three contrasting spreading segments of the Mid-Atlantic Ridge, 33.5°–35°N, *J. Geophys. Res.*, *105*, 8205–8226, doi:10.1029/1999JB900442.

John, B. E., and M. J. Cheadle (2010), Deformation and alteration associated with oceanic and continental detachment fault systems: Are they similar?, in *Diversity of Hydrothermal Systems on Slow Spreading Ocean Ridges*, pp. 175–205, AGU, Washington, D. C., doi:10.1029/2008GM000772.

Karson, J. A. (1998) Internal structure of oceanic litho- sphere: A perspective from tectonic windows, in *Faulting and Magmatism at Mid-Ocean Ridges, Geophys. Monogr. 106*, edited by W. Buck et al., pp. 177–218, AGU, Washington, D. C.

Katz, R. F., M. Spiegelman, and S. M. Carbotte (2004), Ridge migration, asthenospheric flow and the origin of magmatic segmentation in the global mid-ocean ridge system, *Geophys. Res. Lett.*, *31*, L15605, doi:10.1029/2004GL020388.

Kuo, B., and D. W. Forsyth (1988), Gravity anomalies of the ridge-transform system in the South Atlantic between 31° and 34.5°S: Upwelling centers and variations in crustal thickness, *Mar. Geophys. Res.*, *10*, 205–232, doi:10.1007/BF00310065.

Kuznetsov, K., G. Cherkashev, A. Lein, V. Shilov, F. Maksimov, K. Arslanov, and D. Tarasenko (2006), 230Th/U dating of massive sulfides from the Logatchev and Rainbow hydrothermal fields (Mid-Atlantic Ridge), *Geochronometria*, *25*(5), 51–55.

Lavier, L. L., W. R. Buck, and A. N. Poliakov (1999), Self-consistent rolling-hinge model for the evolution of large-offset low-angle normal faults, *Geology*, *27*(12), 1127–1130, doi:10.1130/0091-7613(1999)027<1127:SCRHMF>2.3.CO;2.

Maccaferri, F., E. Rivalta, D. Keir, and V. Acocella (2014), Off-rift volcanism in rift zones determined by crustal unloading, *Nat. Geosci.*, *7*(4), 297–300.

Macdonald, K. C., S. P. Miller, S. P. Huestis, and F. N. Spiess (1980), Three-dimensional modeling of a magnetic reversal boundary from inversion of deep-tow measurements, *J. Geophys. Res.*, *85*, 3670–3680, doi:10.1029/JB085iB07p03670.

MacLeod, C. J., Searle, R. C., Murton, B. J., Casey, J. F., Mallows, C., Unsworth, S. C., Harris, M. (2009), Life cycle of oceanic core complexes, *Earth Planet. Sci. Lett.*, *287*(3), 333–344, doi:10.1016/j.epsl.2009.08.016.

Micallef, A., C. Berndt, D. G. Masson, and D. A. Stow (2007), A technique for the morphological characterization of submarine landscapes as exemplified by debris flows of the Storegga Slide, *J. Geophys. Res.*, *112*, F02001, doi:10.1029/2006JF000505.

Minshull, T. A., M. R. Muller, C. J. Robinson, R. S. White, and M. J. Bickle (1998), Is the oceanic Moho a serpentinization front?, in *Modern Ocean Floor Processes and the Geological Record, Spec. Publ. 148*, edited by R. A. Mills and K. Harrison, pp. 71–80, Geol. Soc., London, U. K., doi:10.1144/GSL.SP.1998.148.01.05.

Morris, E., and R. S. Detrick (1991), Three-dimensional analysis of gravity anomalies in the Mark Area, Mid-Atlantlc Ridge 23° N, *J. Geophys. Res.*, *96*, 4355–4366, doi:10.1029/90JB02173.

Needham, H. D., G. A. Auffret, V. Ballu, P. Beuzart, O. Dauteuil, R. Detrick, and H. Bougault (1991), The crest of the Mid-Atlantic Ridge between 40°N and 15°N: Very broad swath mapping with the EM12 echosounding system, *Eos Trans. AGU*, *72*, 44.

Neves, M. C., M. H. P. Bott, and R. C. Searle (2004), Patterns of stress at mid-ocean ridges and their offsets due to seafloor subsidence, *Tectonophysics*, *386*(3), 223–242, doi:10.1016/j.tecto.2004.06.010.

Olive, J. A., M. D. Behn, and B. E. Tucholke (2010), The structure of oceanic core complexes controlled by the depth distribution of magma emplacement, *Nat. Geosci.*, *3*(7), 491–495, doi:10.1038/ngeo888.

Parker, R. (1973), The rapid calculation of Potential Anomalies, *Geophys. J. R. Astron. Soc.*, *31*, 447–455, doi:10.1111/j.1365-246X.1973.tb06513.x.

Parker, R. L., and S. P. Huestis (1974), The inversion of magnetic anomalies in the presence of topography, *J. Geophys. Res.*, *79*, 1587–1593.

Parson, L., E. Gràcia, D. Coller, C. German, and D. Needham (2000), Second-order segmentation; the relationship between volcanism and tectonism at the MAR, 38°N-35°40′N, *Earth Planet. Sci. Lett.*, *178*(3), 231–251, doi:10.1016/S0012-821X(00)00090-X.

Phipps-Morgan, J., and D. W. Forsyth (1988), Three-dimensional flow and temperature perturbations due to a transform offset: Effects on oceanic crustal and upper mantle structure, *J. Geophys. Res.*, *93*, 2955–2966, doi:10.1029/JB093iB04p02955.

Rabain, A., M. Cannat, J. Escartín, G. Pouliquen, C. Deplus, and C. Rommevaux-Jestin (2001), Focused volcanism and growth of a slow spreading segment (Mid-Atlantic Ridge, 35°N), *Earth Planet. Sci. Lett.*, *185*(1–2), 211–224, doi:10.1016/S0012-821X(00)00371-X.

Reston, T. J., and C. R. Ranero (2011), The 3-D geometry of detachment faulting at mid-ocean ridges. *Geochem. Geophys. Geosyst.*, *12*, Q0AG05, doi:10.1029/2011GC003666.

Rommevaux, C., C. Deplus, P. Patriat, and J. C. Sempéré (1994), Three-dimensional gravity study of the Mid-Atlantic Ridge: Evolution of the segmentation between 28° and 29°N during the last 10 my, *J. Geophys. Res.*, *99*, 3015–3029, doi:10.1029/93JB02361.

Rouzo, S., M. Rabinowicz, and A. Briais (1995), Segmentation of mid-ocean ridges with an axial valley induced by small-scale mantle convection, *Nature*, *374*, 795–798, doi:10.1038/374795a0.

Sauter, D., M. Cannat, S. Rouméjon, M. Andreani, D. Birot, A. Bronner, and R. Searle (2013), Continuous exhumation of mantle-derived rocks at the Southwest Indian Ridge for 11 million years, *Nat. Geosci.*, *6*(4), 314–320, doi:10.1038/ngeo1771.

Schouten, H., H. J. Dick, and K. D. Klitgord (1987), Migration of mid-ocean-ridge volcanic segments, *Nature*, *326*, 835–839, doi:10.1038/326835a0.

Schroeder, T., M. J. Cheadle, H. J. Dick, U. Faul, J. F. Casey, and P. B. Kelemen (2007), Nonvolcanic seafloor spreading and corner-flow rotation accommodated by extensional faulting at 15 N on the Mid-Atlantic Ridge: A structural synthesis of ODP Leg 209, *Geochem., Geophys. Geosyst.*, *8*, Q06015, doi:10.1029/2006GC001567.

Searle R. C., and J. Escartín (2004), The rheology and morphology of oceanic lithosphere and mid-ocean ridges, in *Mid-Ocean Ridges: Hydrothermal Interactions Between the Lithosphere and Oceans*, vol. 148, edited by C. R. German, J. Lin, and L. M. Parson, pp. 63–93, AGU, Washington, D. C., doi:10.1029/148GM03.

Seher, T., W. C. Crawford, S. C. Singh, M. Cannat, V. Combier, and D. Dusunur (2010), Crustal velocity structure of the Lucky Strike segment of the Mid-Atlantic Ridge at 37°N from seismic refraction measurements, *J. Geophys. Res.*, *115*, B03103, doi:10.1029/2009JB006650.

Severinghaus, J. P., and K. C. Macdonald (1988), High inside corners at ridge-transform intersections, *Mar. Geophys. Res.*, *9*(4), 353–367, doi:10.1007/BF00315005.

Shaw, P. R. (1992), Ridge segmentation, faulting and crustal thickness in the Atlantic Ocean, *Nature*, *358*, 490–493, doi:10.1038/358490a0.

Shaw, P. R., and J. Lin (1993), Causes and consequences of variations in faulting style at the Mid-Atlantic Ridge, *J. Geophys. Res.*, *98*, 21,839–21,851, doi: 10.1029/93JB01565.

Smith, D. K., J. R. Cann and J. Escartín (2006), Widespread active detachment faulting and core complex formation near 13°N on the Mid-Atlantic Ridge, *Nature*, *442*(7101), 440–443, doi:10.1038/nature04950.

Smith, D. K., J. Escartín, H. Schouten, and J. R. Cann (2008), Fault rotation and core complex formation: Significant processes in seafloor formation at slow-spreading mid-ocean ridges (Mid-Atlantic Ridge, 13–15°N), *Geochem. Geophys. Geosyst.*, *9*, Q03003, doi:10.1029/2007GC001699.

Spencer, S., D. K. Smith, J. R. Cann, J. Lin, and M. E. D. Ward (1997), Structure and stability of non-transform discontinuities on the Mid-Atlantic Ridge between 24°N and 30°N, *Mar. Geophys. Res.*, *19*(4), 339–362, doi:10.1023/A:1004200411959.

Szitkar, F., J. Dyment, Y. Fouquet, C. Honsho, and H. Horen (2014), The magnetic signature of ultramafic-hosted hydrothermal sites, *Geology*, vol. 42, pp. 715–718, doi:10.1130/G35729.1.

Thibaud R., P. Gente, and M. Marcia (1998), A systematic analysis of the Mid-Atlantic Ridge morphology and gravity between 15°N and 40°N: Constraints of the thermal structure, *J. Geophys. Res.*, *103*, 24,201–24,221, doi:10.1029/97JB02934.

Tivey, M. A., and J. Dyment (2010), The magnetic signature of hydrothermal systems in slow spreading environments, in *Diversity of Hydrothermal Systems on Slow Spreading Ocean Ridges*, pp. 43–66, AGU, Washington, D. C., doi:10.1029/2008GM000773.

Tivey, M. A., and B. E. Tucholke (1998), Magnetization of 0–29 Ma ocean crust on the Mid-Atlantic Ridge, 25° 30′ to 27° 10′ N, *J. Geophys. Res.*, *103*, 17,807–17,826, doi:10.1029/98JB01394.

Tolstoy, M., A. J. Harding, and J. A. Orcutt (1993), Crustal thickness on the Mid-Atlantic Ridge: Bull's-eye gravity anomalies and focused accretion, *Science*, *262*, 726–729, doi:10.1126/science.262.5134.726.

Tucholke, B. E., and J. Lin (1994), A geological model for the structure of ridge segments in slow spreading ocean crust, *J. Geophys. Res.*, *99*, 11,937–11,958, doi:10.1029/94JB00338.

Tucholke, B. E., M. D. Behn, W. R. Buck, and J. Lin (2008), Role of melt supply in oceanic detachment faulting and formation of megamullions, *Geology*, *36*(6), 455–458.

Wessel, P., W. H. F. Smith, R. Scharroo, J. F. Luis, and F. Wobbe (2013), Generic Mapping Tools: Improved version released, *Eos Trans. AGU*, *94*, 409–410.

Wilson, M. F., B. O'Connell, C. Brown, J. C. Guinan, and A. J. Grehan (2007), Multiscale terrain analysis of multibeam bathymetry data for habitat mapping on the continental slope, *Mar. Geod.*, *30*(1-2), 3–35, doi:10.1080/01490410701295962.

AGU PUBLICATIONS

G-cubed

Supporting Information for

Heterogeneous and asymmetric crustal accretion: new constraints from multi-beam bathymetry and potential field data from the Rainbow area of the Mid-Atlantic Ridge (36°15'N)

M. Paulatto[1,2], J. P. Canales[3], R. A. Dunn[4] and R. A. Sohn[3]

[1]Géoazur, Université Nice Sophia Antipolis, [2]Department of Earth Sciences, University of Oxford, [3]Woods Hole Oceanographic Institution, [4]Dept. of Geology and Geophysics, School of Ocean and Earth Science and Technology, University of Hawaii at Manoa

Contents of this file

1. Introduction

This supporting information provides additional details on the data processing and a figure displaying data coverage.

2. Data processing

2.1 Swath bathymetry

The swath bathymetry data were collected with a Kongsberg EM-122 multi-beam system transmitting at a frequency of 12 kHz. The angular coverage was initially set to 130 degrees and later reduced to 124 degrees to improve data from the outer beams. The resulting swath width is ~3.5 times the water depth, corresponding to 1500 - 12,000 m in our survey area. The varying profile spacing, dictated by the design of the seismic experiment, resulted in redundant swath coverage in the central parts of the survey area and sparser coverage in the outer regions (see Fig. S1a,b). The data were hand edited to remove artifacts using MB-System [*Caress and Chayes*, 1996; www.mbari.org/data/mbsystem] and were then exported and gridded using a continuous curvature algorithm [*Wessel et al.,* 2013]. The data were merged with existing data from previous cruises [*Needham et al.,* 1991; *Detrick et al.,* 1995; *Cannat et al.,* 1999], with priority given to the MARINER data. The high density of soundings allowed gridding at a relatively fine grid interval of 0.00025ºx0.00025º (~25 m grid spacing).

2.2 Gravity data

The gravity data were recorded with a Bell Aerospace BGM-3 marine gravimeter consisting of a force-balance vertical accelerometer mounted on a gyro-stabilized free rotating platform. The sensor is axis-symmetric and does not require cross-coupling error correction [*Bell and Watts*, 1986]. The gravity data were processed with navigation data to correct for the Eötvös effect, which is calculated from the ship's latitude, heading and speed. The processed gravity data were corrected for instrument drift and converted to absolute measurements by performing a tie with gravity base stations in St. George (Bermuda) and Ponta Delgada (Azores). The free-air gravity anomaly was then calculated by subtracting the drift-adjusted processed gravity data from the 1984 international gravity formula for a rotating ellipsoid with flattening of 1/298.25 (Fig. 3a). The free-air gravity anomaly was filtered with a 600 s Gaussian filter to remove short-period noise introduced from scatter in the Eötvös correction arising from uncertainties in the ship's attitude data [e.g. *Paulatto et al.,* 2014]. The free-air anomaly was merged with data from previous cruises available from the NGDC and Sismer databases [*Detrick et al.,* 1995; *Cannat et al.,* 1999; *Escartin et al.*, 2001] and gridded using b-spline polynomials and a regular grid spacing of 0.002 degrees (see Fig. S1c for data coverage).

2.3 Magnetic data

The magnetic data were recorded with a Geometrics G-882 cesium vapor magnetometer towed 140 m astern of the ship along a series of profiles during the seismic experiment. The magnetic data were corrected for the instrument layback and filtered with a 20 s median filter to remove short-wavelength noise. The magnetic field values were then converted to magnetic anomalies by removing the International Geomagnetic Reference Field (IGRF). The resulting values were merged with data from previous cruises available from the NGDC and Sismer databases [*Tivey and Dyment*, 2010] and were gridded using b-spline polynomials and a grid spacing of 0.002 degrees (see Fig. S1d for data coverage).

References

Bell, R. E. and A. B. Watts (1986), Evaluation of the BGM-3 sea gravity meter system onboard R/V Conrad, *Geophysics*, 51 (7), 1480-1493.

Cannat, M., Briais, A., Deplus, C., Escartín, J., Georgen, J., Lin, J., and da Silva, P. (1999), Mid-Atlantic Ridge–Azores hotspot interactions: along-axis migration of a hotspot-derived event of enhanced magmatism 10 to 4 Ma ago, *Earth Planet. Sc. Lett.*, *173*(3), 257-269.

Caress, D. W., and D. N. Chayes (1996), Improved processing of Hydrosweep DS Multibeam Data on the R/V Maurice Ewing, *Mar. Geophys. Res.*, 18, 631-650.

Detrick, R. S., Needham, H. D., and Renard, V. (1995), Gravity anomalies and crustal thickness variations along the Mid-Atlantic Ridge between 33ºN and 40ºN, *J. Geophys. Res.*, *100*(B3), 3767-3787.

Escartín, J., Cannat, M., Pouliquen, G., Rabain, A., and Lin, J. (2001), Crustal thickness of V-shaped ridges south of the Azores: Interaction of the Mid-Atlantic Ridge (36–39ºN) and the Azores hot spot, *J. Geophys. Res.*, *106*(B10), 21719-21735.

Needham, H. D., Auffret, G. A., Ballu, V., Beuzart, P., Dauteuil, O., Detrick, R., Bougault, H. (1991), The crest of the Mid-Atlantic Ridge between 40ºN and 15ºN: Very broad swath mapping with the EM12 echosounding system, *Eos Trans. AGU*, *72*, 44.

Paulatto, M., Watts, A. B., & Peirce, C. (2014), Potential field and bathymetric investigation of the Monowai volcanic centre, Kermadec Arc: implications for caldera

formation and volcanic evolution, *Geophys. J. Int.*, *197*(3), 1484-1499, doi:10.1093/gji/ggt512.
Tivey, M. A., and Dyment, J. (2010), The magnetic signature of hydrothermal systems in slow spreading environments, In *Diversity of Hydrothermal Systems on Slow Spreading Ocean Ridges*, 43-66.
Wessel, P., W. H. F. Smith, R. Scharroo, J. F. Luis, and F. Wobbe (2013), Generic Mapping Tools: Improved version released, *EOS Trans. AGU*, 94, 409-410.

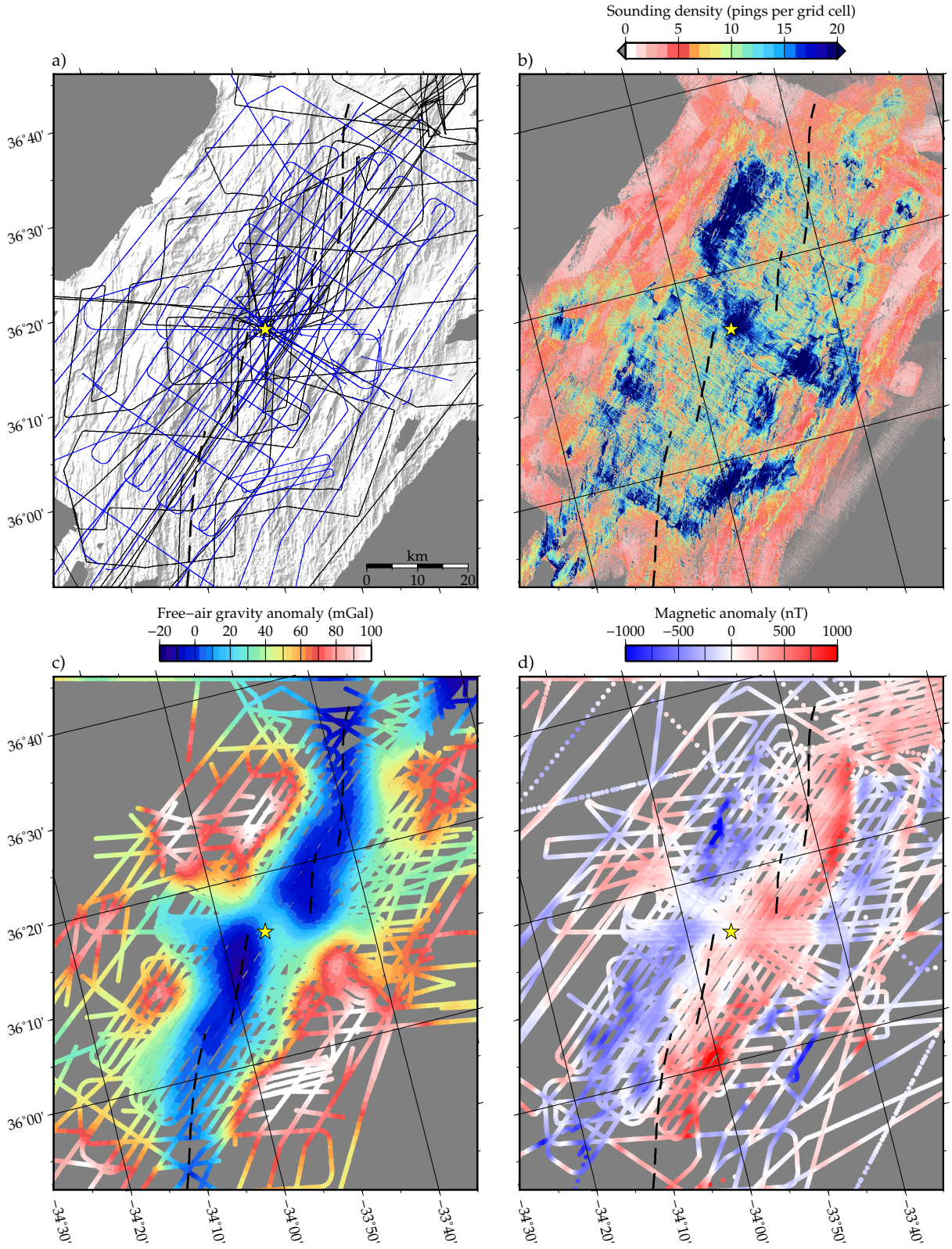

Figure S1. a) Blue: Ship track of cruise MGL1305. Only the sections with swath bathymetry data used to produce the bathymetry grid are plotted. Black: Ship tracks of

other cruises used in the swath bathymetry compilation. b) Coverage of swath bathymetry data represented as number of swath soundings in each 0.00025ºx0.00025º cell for the combined swath bathymetry compilation. c) Gravity data. Free-air gravity anomaly plotted as a small circle (500 m radius) for each individual measurement in the assembled compilation. d) Magnetic data. Magnetic anomaly plotted as a small circle (500 m radius) for each individual measurement in the assembled compilation. In all panels the map projection is rotated to align the horizontal with the spreading direction. A dashed black line marks the ridge axis. The Rainbow hydrothermal field is marked by a yellow star.